Reconsideration of winds, wind waves, and turbulence in simulating wind-driven currents of shallow lakes in the Wave-current Coupled Model (WCCM) version 1.0

Tingfeng Wu[1], Boqiang Qin[1], Anning Huang[2], Yongwei Sheng[3], Shunxin Feng[4], Céline Casenave[5]

[1]Nanjing Institute of Geography and Limnology, Chinese Academy of Sciences, Nanjing, Jiangsu 210008, P.R. China
[2]School of Atmospheric Sciences, Nanjing University, Nanjing 210023, P.R. China
[3]Department of Geography, University of California, Los Angeles, CA 90095, USA
[4]China Institute of Water Resources and Hydropower Research, Beijing 100038, P.R. China
[5]MISTEA, University of Montpellier, INRAE, Institut Agro, Montpellier, France

Correspondence to: Boqiang Qin (qinbq@niglas.ac.cn)

Abstract. Winds, wind waves, and turbulence are essential variables and playing critical role in regulating a series of physical and biogeochemical processes in large shallow lakes. However, parameterizing winds, waves, currents and turbulence and simulating the interaction between them in large shallow lakes haven't been evaluated strictly because of a lack of field observations of lake hydrodynamics process. To address this problem, two process-based field observations were conducted to record the development of summer and winter wind-driven currents in Lake Taihu, a large shallow lake in China. Based on these observations and numerical experiments, a wave-current coupled model (WCCM) is developed by rebuilding expression of wind drag coefficient, introducing wave-induced radiation stress, and adopting a simple turbulence scheme, and then used to simulate wind-driven currents in Lake Taihu. The results show that, the WCCM can accurately simulate the upwelling process resulting from the wind-driven currents during the field observations. Comparing with other model, there is a 42.9% increase of WCCM-simulated current speed which is mainly attributed to the new expression of wind drag coefficient. Meanwhile WCCM-simulated current direction and field are also improved due to the introduction of wave-induced radiation stress. Furthermore, the use of the simple turbulent scheme in the WCCM makes the simulation of the upwelling processes more efficient. The WCCM provides a sound basis for simulating shallow lake ecosystems.

Keywords. shallow lake, process-based observation, three-dimensional wind-driven current model, winds, wind waves, turbulence

1 Introduction

Three-dimensional hydrodynamic models are efficient tools to deeply understand currents at large scale and the basis to develop water quality models. Generally, these three-dimensional hydrodynamic models are developed based on the Naiver-Stokes equations and solved the equations using a split-explicit method (Blumberg and Mellor, 1987), such as Regional Oceanic Modeling System (ROMS; Shchepetkin et al., 2005); Environmental Fluid Dynamics Computer Code (EFDC;

Hamrick, 1992); Finite-Volume Coastal Ocean Model (FVCOM; Chen et al., 2011). However, all these models are initially developed based in marine environments. They can not be directly applied to simulate the currents of inland lakes with limited water depth and fetch (Sterner et al., 2017; Lükő et al., 2020) until some essential variables in these models are reconsidered according to the characteristics of lacustrine hydrodynamics, such as winds (wind drag coefficient), wind

35   waves (wave-induced radiation stress), and turbulence (vertical eddy viscosity).

In large water bodies, winds is the main stress for driving currents (Hutter et al., 2011; MacIntyre et al., 2020; Rey et al., 2021; Schoen et al., 2014). Wind stress on water surface is always a hotspot for the hydrodynamic study (Jeffreys, 1925; Munk, 1955; Wu, 1980; Shchepetkin and McWilliams, 2005; Chen et al., 2020). Usually, the energy transfer efficiency of wind is represented by the wind drag coefficient, which is a constant or linear function of the wind speed (Large and Pond,

40   1981; Hamrick, 1992; Huang et al., 2010). However, recent field observations in large lakes imply that the change of the wind drag coefficient is discontinuity (Lükő et al., 2020; Xiao et al., 2013). They suggested that the drag coefficient taken from experimental studies conducted in the open oceans may be subject to large uncertainties when applied to inland lakes.

Similarly, wind waves can influence the development of wind-driven currents (Ji et al., 2017), but numerical models applied to large lakes seldom consider this wind wave effect. The development of wind waves can affect the generation of wind-

45   induced currents by altering the wind momentum transmission efficiency at the air-water interface (Chen, et al., 2020; Foken, 2008; Wei, et al., 2016; Wüest & Lurke, 2003) and stress equilibrium below the surface waves (Ardhuin et al., 2008; Longuet-Higgins and Stewart, 1964; Sun et al., 2006; Xu and Bowen, 1994). Recently, some models have been revised to consider this wind wave effect represented by wave-induced radiation stress in ocean environments, such as ROMS (Kumar et al., 2011; Warner et al., 2008) and FVCOM (Wu et al., 2011). However, few numerical researches have considered the

50   wind wave effect in large lakes, despite that the importance of wind waves for large lake ecosystems is widely proved during last two decades, especially for large shallow lakes (Hofmann et al., 2008; Jin and Ji, 2005; Vinçon-Leite and Casenave, 2019; Wu et al., 2019).

The lag of the development of the lake current models is mainly due to a lack of process-based field observations of lake hydrodynamics, which can provide the model development with measured time series of hydrodynamic changes resulted

55   from an external stress event, such as wind stress (Huang et al., 2010; Lükő et al., 2020; MacIntyre et al., 2020; Wu et al., 2018). However, few model researches take the process-based observation so that the applicability of most hydrodynamics models to large lakes has not been verified strictly. This is because of the harsh working environment and uncertainty of timing of strong wind events at the best time to observe the development of wind-driven currents (Zhou et al., Wu et al., 2018). The lack of the process-based field observations also impedes us to determine the optimal turbulence scheme for large

60   lakes.

To this end, two process-based field observations were conducted to collect time series of hydrodynamics during two strong wind events in Lake Taihu, a large shallow lake in eastern China. Based on these time series, we developed a two-way coupled hydrodynamic-wave numerical model (Wave-Current Coupled Model: WCCM) with reconsideration of description of winds, wind waves, and turbulence to simulate the wind-driven currents in Lake Taihu. We will answer two questions as

65 follows: (1) Can the performance of the hydrodynamic model in simulating the wind-driven currents of large shallow lakes be obviously improved by adopting the new schemes of wind stress, wind waves and turbulence? (2) What are the contributions of winds, waves, and turbulence to improve the simulation of wind-driven currents and underlying mechanisms?

2 Introduction

2.1 Study area

70 Lake Taihu ($30°55'40''$–$31°32'58''$N, $119°52'32''$–$120°36'10''$E) is a large, shallow, and dish-shaped lake located in the Yangtze River delta plain in China (Fig. 1). It covers an area of 2339 km2 with an average water depth of 1.9 m and an average lakebed slope of $19.7''$. The wind field over the lake is mainly affected by the East Asian monsoon. The multi-year average wind speed is 3.4 ± 0.19 m s^{-1}. southeast-east winds prevail from April to August, while north-northwest winds dominate in the other months. The basin-scale hydrodynamics is mainly determined by winds rather than inflow-outflow (Li

75 et al., 2011; Wu et al., 2018; Zhao et al., 2012). Except temporary small vertical water temperature gradient, Lake Taihu is mixed evenly along water depth because of frequent disturbance of winds (Wu et al., 2018). Several numerical models have been used to simulate the wind-driven currents and their influence on the ecological processes in Lake Taihu (Feng et al., 2018; Han, et al., 2019; Li et al., 2015; Zhao et al., 2012), but the hydrodynamic part of these models was not evaluated using the process-based field observation.

80 ### 2.2 Process-based field observations

Two process-based field observations were made in Lake Taihu in summer 2015 (from 0:00 on August 1 to 0:00 on August 12, 2015) and winter 2018 (from 0:00 on December 19 to 0:00 on December 31, 2018), respectively. Five water level stations (WL1–WL5; Fig. 1) around Lake Taihu built by the Ministry of Water Resources of the People's Republic of China recorded the water level at 60-min intervals. A portable weather station (WXT520; Vaisala Inc., Finland) and an acoustic

85 Doppler profiler (ADP; SonTek Inc., USA) (LCWS) were deployed at the Lake Current and Weather Station (LCWS, Fig. 1) for the lake current and weather measurements simultaneously, including surface air pressure, wind speed and direction, air temperature, and relative humidity at 10-min intervals, current velocity profiles and water temperature at 30 min intervals with an accuracy of ±0.5 cm s^{-1} and ±0.1 °C. In addition, hourly solar radiation and cloud cover data were collected from the station of Taihu Laboratory for Lake Ecosystem Research (TLLER).

90 ## 3 Wave-current coupled model

The WCCM is developed by two-way coupling a three-dimensional lake current model (LCM) with the Simulating WAves Nearshore model (SWAN; Booij and Holthuijsen, 1999).

3.1 Three-dimensional lake current model

The LCM is developed to simulate the water level and lake currents.

95 ### 3.1.1 Governing equations

The governing equations for lake currents in the Cartesian coordinate system (Fig. 2) consist of the continuity equation and momentum equations (Koue et al., 2018). To eliminate the influence of lakebed topography on the lake current simulations, the sigma (σ) coordinate system is introduced in the vertical direction (Fig. 2).

Based on the rule of derivation of a composite function, the continuity equation and momentum equation in the Cartesian
100 coordinate system (x', y', z, t') are transformed into the σ coordinate system (x, y, σ, t) using Eqs. A1-1 to A1-5.

$$\frac{\partial(Hu)}{\partial x} + \frac{\partial(Hv)}{\partial y} + \frac{\partial(Hw)}{\partial \sigma} + \frac{\partial \zeta}{\partial t} = 0 \ , \tag{1}$$

$$\frac{\partial(Hu)}{\partial t} + \frac{\partial(Huu)}{\partial x} + \frac{\partial(Huv)}{\partial y} + \frac{\partial(Huw)}{\partial \sigma} = fHv + F_x H - \frac{\rho g H}{\rho_0}\frac{\partial \zeta}{\partial x} + H\frac{\partial}{\partial x}\left(A_H \frac{\partial u}{\partial x}\right) + H\frac{\partial}{\partial y}\left(A_H \frac{\partial u}{\partial y}\right) + \frac{1}{H}\frac{\partial}{\partial \sigma}\left(A_v \frac{\partial u}{\partial \sigma}\right) + \varepsilon_U \ , \tag{2}$$

$$\frac{\partial(Hv)}{\partial t} + \frac{\partial(Huv)}{\partial x} + \frac{\partial(Hvv)}{\partial y} + \frac{\partial(Hvw)}{\partial \sigma} = -fHu + F_y H - \frac{\rho g H}{\rho_0}\frac{\partial \zeta}{\partial y} + H\frac{\partial}{\partial x}\left(A_H \frac{\partial v}{\partial x}\right) + H\frac{\partial}{\partial y}\left(A_H \frac{\partial v}{\partial y}\right) + \frac{1}{H}\frac{\partial}{\partial \sigma}\left(A_v \frac{\partial v}{\partial \sigma}\right) + \varepsilon_V \ , \tag{3}$$

Where: u, v, and w are the components of the current velocity in the x-, y-, and σ-directions (m s^{-1}, m s^{-1}, s^{-1}), respectively; h,
105 ζ, and H are the lakebed elevation, water level, and water depth (m), respectively; f is the Coriolis force (s^{-1}) defined by $f = 2\omega\sin\varphi$, where ω is the rotational angular velocity of the earth and φ is the geographic latitude; F_x and F_y are the wave-induced radiation stress in the x- and y-directions, respectively; ρ and ρ_0 are the water and reference density (kg m^{-3}), respectively; g is the gravitational acceleration; A_H and A_V are the horizontal and vertical eddy viscosity (m^2 s^{-1}), respectively; and ε_U, and ε_v, are the secondary terms introduced by the coordinate system transformation (Eqs. A2-1 to A2-6).

110 ### 3.1.2 Turbulence scheme

To improve the calculation efficiency, the value of the vertical eddy viscosity (A_V) is estimated using the Prandtl length l and the Richardson number (R_i).

$$A_V = \left(5 \times 10^{-6} + \frac{l^2}{H}\sqrt{\left(\frac{\partial u}{\partial \sigma}\right)^2 + \left(\frac{\partial v}{\partial \sigma}\right)^2}\right)(1 + 0.1R_i)^{-1} \ , \tag{4}$$

l and R_i are given by:

115 $$l = \kappa(\sigma H + z_0)\left(1 - \frac{\sigma}{1+r_S}\right) , \tag{5}$$

$$R_i = -\frac{g}{\rho}\frac{\partial \rho}{\partial z}\left(\left(\frac{\partial u}{\partial \sigma}\right)^2 + \left(\frac{\partial v}{\partial \sigma}\right)^2\right)^{-1} , \tag{6}$$

where κ is the von Kármán constant, z_0 is the roughness height of the lakebed, and r_s is the roughness height of the lake surface.

4

3.1.3 Boundary conditions

120 Wind stress at the lake surface:

$$\frac{\rho A_V}{H}\left(\frac{\partial u}{\partial \sigma}, \frac{\partial v}{\partial \sigma}\right) = \rho_a C_s \sqrt{u_w^2 + v_w^2}\,(u_w, v_w)\,, \tag{7}$$

where ρ_a is the air density, u_w and v_w are the wind speed components in the x- and y-directions at 10 m above the lake surface (m s^{-1}), respectively, and C_s is the wind drag coefficient.

Here, according to the process-based observations and model calibration described in the following section 4.1, we define a

125 new expression of C_s that considers the discontinuity of changing trend and directionality of wind momentum transmission, which differs from previously reported expressions of C_s.

$$x\text{-direction: } C_s = \begin{cases} 0.00046\left(\frac{35}{0.1+e^{4-0.1|u_w|}} + 0.25\right) & |u_w| \geq 7.5 \\ 0.00074 & |u_w| < 7.5 \end{cases}, \tag{8}$$

$$y\text{-direction: } C_s = \begin{cases} 0.00046\left(\frac{35}{0.1+e^{4-0.1|v_w|}} + 0.25\right) & |v_w| \geq 7.5 \\ 0.00074 & |v_w| < 7.5 \end{cases}, \tag{9}$$

Friction at the lakebed:

130 $$\frac{\rho A_V}{H}\left(\frac{\partial u}{\partial \sigma}, \frac{\partial v}{\partial \sigma}\right) = \rho C_B \sqrt{u^2 + v^2}\,(u, v)\,, \tag{10}$$

where C_B is the bottom friction coefficient that is given by:

$$C_B = \left(\frac{\kappa}{\ln\left(\frac{\sigma_b H + z_0}{z_0}\right)}\right)^2\,, \tag{11}$$

3.1.4 Wave-induced radiation stress

Wave-current interaction is a complicated process (Mellor, 2008). Up to now, it is not fully understood. Longuet-Higgins

135 and Stewart (1964) firstly proposed the concept of wave-induced radiation stress and Sun et al. (2006) derived the expressions of the stress for three-dimensional current numerical models:

$$F_w = -\frac{\partial}{\partial x}\left[\frac{\pi g H_S^2 \omega \cos \varphi}{2L}\sin\theta_1 \frac{\sinh\left(\frac{4\pi\sigma H}{L}\right)}{\sinh\left(\frac{4\pi H}{L}\right)}\right] + \frac{\partial}{\partial y}\left[\frac{\pi g H_S^2}{2L}\frac{\sinh^2\left(\frac{2\pi\sigma H}{L}\right)}{\sinh\left(\frac{4\pi H}{L}\right)}\right] - \frac{\pi g H_S^2 T_0 \omega \sin\varphi \cosh\left(\frac{4\pi\sigma H}{L}\right)}{L^2 \sinh\left(\frac{4\pi H}{L}\right)}\,, \tag{12}$$

$$F_x = F_w \sin\left(\theta_m - \frac{\pi}{2}\right)\,, \tag{13}$$

$$F_y = F_w \cos\left(\theta_m - \frac{\pi}{2}\right)\,, \tag{14}$$

140 where H_S is the significant wave height (m), T_0 is the wave period (s), L is the wavelength (m), θ_m is the mean wave direction, and θ_1 is the angle between the mean wave direction and geographical east direction.

3.1.5 Solution of equations

The splitting mode technique (Blumberg and Mellor, 1987) and alternation direction implicit difference scheme (Butler, 1980) are used to discretize the Equations (1 to 3) on the staggered grid (Figs. 2 and 3). The detailed description of the solution of equations is indicated in Appendix A3.

3.2 Simulating WAves Nearshore model

In view of the importance of wind waves in the hydrodynamic and ecological processes of shallow lakes, the SWAN model, which has been proven suitable for simulating the wind waves in Lake Taihu (Wang et al., 2016; Wu et al., 2019; Xu et al., 2013) was used to simulate the spatiotemporal variation of wind waves in the lake. The governing equation for SWAN is the wave action balance equation:

$$\frac{\partial N}{\partial t} + \frac{\partial c_x N}{\partial x} + \frac{\partial c_y N}{\partial y} + \frac{\partial c_{\sigma_1} N}{\partial \sigma_1} + \frac{\partial c_\theta N}{\partial \theta} = \frac{S}{\sigma_1},$$

(15)

where N is the action density spectrum, t, x, and y are the time and horizontal coordinate directions, respectively, σ_1 is the relative frequency, θ is the wave direction, c_x, c_y, c_{σ_1}, and c_θ denote the wave propagation velocity in x, y, σ_1, and θ space, respectively, and S is the source in terms of energy density representing the effects of generation, dissipation, and nonlinear wave-wave interactions. H_S, T_0, L and θ_m are deduced from the value of $N(x, y, t, \sigma_1, \theta)$ (Booij et al., 2004).

The action balance equation is solved in the Cartesian coordinate system using the first-order upwind scheme of the finite difference method (Booij and Holthuijsen, 1999; Booij et al., 2004).

3.3 Two-way coupling of the LCM with SWAN

SWAN and LCM were coupled together to establish the WCCM model (Fig. 3). The current speeds u and v, and the water level ζ that are computed by the LCM model are inputs of the SWAN model. On the other hand, H_S, T_0, L and θ_m that are computed by the SWAN model are used as inputs in the LCM model, for the computation of the wave induced radiation stresses F_x and F_y (Eqs. (13) and (14)).

3.4 Configuration of the WCCM in Lake Taihu

The WCCM is used to simulate the wind waves and lake currents of Lake Taihu during the period of process-based field observations. The computational domain of Lake Taihu (Fig.1) for the LCM is divided in $72 \times 72 = 5184$ cells at 1 km resolution. The water column is divided into five layers in the vertical direction and the time step is 30 s. The value of α is 0.5.

Lake Taihu is considered as a closed lake for the simulation because the influence of inflows and outflows on the current field is very small compared to the influence of the wind stress (Li et al., 2011; Wu et al., 2018; Zhao et al., 2012). The simulations therefore disregard the inflows and outflows. The model inputs at the air-water boundary include air temperature,

surface air pressure, cloud cover, relative humidity, wind speed and direction provided by the LCWS and TLLER stations (Fig. 1). Among them, the measured wind speed at 5 m above the water surface was adjusted to 10 m (Wu et al., 2018) using the method suggested by the Coastal Engineering Research Center (1984). The initial condition for the water level was obtained by interpolation of the values of the water levels measured at stations WL1–WL5 at the beginning of the model

175　integration. The initial water temperature was set to the measured values recorded by the ADP at the beginning of the model integration and the current speed was initialized by 0 m s^{-1}.

Ten parameters need to be determined for the simulation of the LCM (Table 1). Among them, φ, g, κ, and ρ_a are constants, while A_v and C_B values can be calculated from the values of κ, z_0 and r_s. A_H and z_0 values are the same values as the ones used for the EFDC (Environmental Fluid Dynamics Code) and r_s is set to 0.01 (Table 1). Being described in the following section,

180　the EFDC, which is a hydrodynamic numerical model, is used here to evaluate the WCCM's performance. The expression of the wind drag coefficient is designed and calibrated using the process-based observation data of 2015.

The mesh of the SWAN model is the same as the horizontal mesh of the LCM. Considering the randomness of wind waves, the characteristic values of wind waves are typically represented by the statistical values of the high frequency pressure records over a 10-min period. The time increment of the SWAN model was therefore set to 600 s. The frequency band was

185　set to 0.04–4 Hz and the wave direction ranged from 0 ° to 360 ° with an increment of 6 °. The second generation mode was used to calculate the source term (e.g., wind input, depth-induced wave breaking, bottom friction, triads). The parameter *cdrag* of the SWAN model was set to 0.00133 and the Collins bottom friction coefficient was set to 0.025. The calibration and validation of these parameters have been reported in previous studies (Xu et al., 2013; Wang et al., 2016).

Considering the time of the peak of the winds and cold start of the WCCM, the hydrodynamic time series of the latter half of

190　the 2015 observation (from 0:00 on August 8 to 0:00 on August 12, 2015; Summer observation in 2015) were used to calibrate the WCCM and those of the latter half of the 2018 observation (from 0:00 on December 26 to 0:00 on December 31, 2018; Winter observation in 2018) were used to evaluate WCCM's performance.

Because the influence of lake currents on the SWAN-simulated wind waves has already been analyzed in Lake Taihu (Li et al., 2007), only the WCCM simulation of lake currents was evaluated in this study.

195　**3.5 Methods**

3.5.1 Statistical analysis

To evaluate the WCCM model performance, the mean absolute error (*MAE*), the root mean square error (*RMSE*), and the correlation coefficient (*r*) between the measured and simulated values at both significance levels of $p < 0.05$ and $p < 0.01$ are considered (Koue et al., 2018). The magnitude of lake current speed is expressed as the mean ±standard deviation.

200　The mean absolute error of the horizontal current direction (MAE_{UVD}; Carvalho et al., 2012) is used to compare the simulated and measured values:

$$MAE_{\text{UVD}} = \frac{1}{N}\sum_{i=1}^{N}|M_i - O_i| \qquad\qquad |M_i - O_i| < 180^{\text{O}} \ , \tag{16}$$

$$MAE_{\text{UVD}} = \frac{1}{N}\sum_{i=1}^{N}\left|(M_i - O_i)\left(1 - \frac{360}{|M_i - O_i|}\right)\right| \qquad\qquad |M_i - O_i| \geq 180^{\mathrm{O}} \;, \qquad\qquad (17)$$

In addition, ArcGIS 10.2 (ESRI Inc., USA) was used to process the spatial data and Tecplot 360 (Tecplot Inc., USA) was

205 used to draw contours of the water level, current field, and streamtraces.

3.5.2 Comparison between the WCCM and EFDC

Comparison between different models is a useful method to study currents in large water bodies (Huang et al., 2010; Morey et al., 2020). The EFDC is one of the most widely used models for shallow lakes worldwide (Chen et al., 2020) and offers a general-purpose modeling package to simulate three-dimensional flow, transport, and biogeochemical processes in surface

210 water systems (Ji et al., 2001; Ji, 2008). The EFDC has been successfully applied in Lake Taihu modelling (Li et al., 2011; Li et al., 2015; Wang et al., 2013).

The EFDC hydrodynamic model was developed by Hamrick (1992) and its governing equations are the same as Eqs. (1)–(3). It uses the splitting mode technique to solve the continuity equation and momentum equation in the σ coordinate system. The Mellor-Yamada turbulence model is used in EFDC to calculate the vertical eddy viscosity (Ji et al., 2001). The wind stresses

215 in the EFDC is calculated using the following equations (Hamrick, 1992; Li et al., 2015):

$$\left(\tau_{sx}, \tau_{sy}\right) = \frac{\rho_{\mathrm{a}}}{\rho} C_{\mathrm{s}}' \sqrt{u_{\mathrm{w}}^2 + v_{\mathrm{w}}^2}(u_{\mathrm{w}}, v_{\mathrm{w}}) \;, \qquad\qquad (18)$$

$$C_{\mathrm{s}}' = 0.001\left(0.8 + 0.065\sqrt{u_{\mathrm{w}}^2 + v_{\mathrm{w}}^2}\right) \;, \qquad\qquad (19)$$

The mesh used for the simulation with the EFDC is the same as the LCM and WCCM. After consulting the authors of the uncertainty and sensitivity analysis performed on the hydrodynamic parameters of the EFDC for Lake Taihu (Li et al., 2015),

220 the optimal horizontal eddy viscosity was set to 1 $\mathrm{m}^2\ \mathrm{s}^{-1}$, the roughness height to 0.005 m, and w_{s} to 0.7.

3.5.3 Numerical Experiments

Four numerical experiments were designed to evaluate the accuracy of the WCCM and to identify the relative importance of winds, wind waves, and turbulence in improving simulation of the wind-driven currents as follows:

- Experiment 1, denoted EFDC: numerical simulation of the lake currents using the EFDC. In this experiment,
225 the Mellor-Yamada turbulence scheme is used and the drag coefficient is given by Eqs (18)-(19), but the wave-induced radiation stress is not considered (no coupling with SWAN);

- Experiment 2, denoted LCM_1: numerical simulation of the lake currents using the LCM, with the same expression of the drag coefficient as in EFDC (Eqs (18)-(19)), but a different turbulence scheme that is given by Eqs.(4)-(6), and still without consideration of wave-induced radiation stress;

230 - Experiment 3, denoted LCM_2: same experiment as LCM_1 with a different expression of the drag coefficient that is given by Eqs. (8)-(9), still without consideration of wave-induced radiation stress;

- Experiment 4, denoted WCCM: same experiment as LCM_2 but with consideration of wave-induced radiation stress to achieve the two-way coupling model.

4 Results

4.1 Summer observation and model calibration in 2015

The average wind speed over Lake Taihu between 0:00 on August 8 and 0:00 on August 12, 2015 was 8.6 m s^{-1} (Fig. 4) with a maximum of 13.5 m s^{-1} at 13:00 on August 10, corresponding to a wind direction of 107.5°. Lake Taihu experienced a strong southeast-east wind event during the observation.

The mean water level observed at the five stations was 3.64 ± 0.01 m with a maximum of 4.04 m recorded at the WL1 station at 12:00 on August 10 (Fig. 5) corresponding to the 3.38 m recorded at the WL4 station. The mean measured current speeds of the surface, middle, and bottom water layers at the LCWS station (Fig. 6) were 5.0 ± 3.0, 5.5 ± 3.5, and 5.4 ± 3.6 cm s^{-1}, respectively.

The average r values between simulated and measured water levels of EFDC, LCM_1, LCM_2, and WCCM are 0.87, 0.88, 0.86, and 0.86 ($p < 0.01$; Table 2), respectively, and the average $RMSE$ values are 0.05, 0.05, 0.05, and 0.04 m. The average r values between simulated and measured current speeds of EFDC, LCM_1, LCM_2, and WCCM are 0.46, 0.57, 0.61, and 0.66 ($p < 0.01$; Table 3), while the average MAE_{UVD} values are 57°, 57.1°, 56.3°, and 52.9°.

The contours of the water level simulated by the WCCM at 13:00 on August 10, corresponding to the time of the maximum wind speed, are similar to the EFDC simulation and show a decrease trend from northwest to southeast (Fig. 7). The surface current field simulated by these two models mainly flows from southeast to northwest, which can be further demonstrated by the simultaneous stream traces (Fig. B.1). The middle and bottom current fields of the southern part of the lake are consistent with the surface current field, but those in the center and northern parts of the lake mainly flow from southwest to northeast.

A major difference between the WCCM- and EFDC-simulated current fields is in that the current speed simulated by the former is significantly higher (Fig. 7). There are vortexes produced by the WCCM in the upwind area, such as in Xukou Bay and northwest of Xishan Island (Fig. B.1). In contrast, the vortexes simulated by the EFDC tend to be located in the downwind area, such as Zhushan Bay and Meiliang Bay (Fig. B.1).

4.2 Winter observation and model validation in 2018

The average wind speed over Lake Taihu is 8.7 m s^{-1} between 00:00 on December 26 and 00:00 on December 31, 2018 (Fig. 8) with a maximum of 13.6 m s^{-1} at 22:00 on December 26, corresponding to a wind direction of 26.3°. Lake Taihu experienced a strong north-northeast wind event during the observation.

The mean water level over the five stations was 3.46 ± 0.01 m with a minimum of 3.23 m recorded at the WL5 station at 22:00 on December 26 corresponding a secondary peak of 3.62 m recorded at the WL3 station (Fig. 9). The mean measured

surface, middle, and bottom current speeds at the LCWS station (Fig. 10) were 3.7 ± 2.0, 3.5 ± 2.0, and 4.2 ± 2.2 cm s^{-1}, respectively.

The EFDC, LCM_1, LCM_2, WCCM-simulated water levels at each water level station significantly correlate with the

265 measured values ($p < 0.01$; Table 4). The average r values are 0.87, 0.88, 0.88, and 0.87, respectively, and the average $RMSE$ values are 0.04, 0.05, 0.03, and 0.03 m. The average r values between simulated and measured current speed of EFDC, LCM_1, LCM_2, and WCCM are 0.21, 0.22, 0.29, and 0.3 ($p < 0.05$; Table 5), while the average MAE_{UVD} values are 77 °, 77.2 °, 77 °, and 75.7 °.

The water level contours simulated by the WCCM at 22:00 on December 26, 2018, corresponding to the time of the

270 maximum wind speed, are similar with those by the EFDC. They show a decease trend from southwest to northeast (Fig. 11). The surface current fields simulated by these two models mainly flow from north to south, which can be further demonstrated by the simultaneous stream traces (Fig. B.2). The middle and bottom current fields mainly flow from northwest to southeast.

The main difference between the WCCM- and EFDC-simulated current fields is that the current speed simulated by the

275 former is significantly higher (Fig. 11). Clockwise vortexes formed in Gonghu Bay in the surface, middle, and bottom current fields simulated by the EFDC (Fig. B.2), whereas this clockwise vortex is only located in the middle current field simulated by the WCCM.

5 Discussion

Influenced by the strong southeast-east wind event during the summer observation in 2015, the maximum water level

280 difference at 12:00 on August 10 between WL1 located in the downwind lake area and WL4 station located in the upwind lake area was 0.66 m (Fig. 5). Before this maximum, all of the measured surface, middle, and bottom currents flow along wind direction and their speed significantly increased (Fig. 6). It can be concluded that the strong southeast-east winds drive whole water column at the LCWS station to form monolayer wind-driven currents, and then result in a downwind upwelling (Wu et al., 2018). Similarly, generated by the strong north-northeast wind event during the winter observation in 2018, wind-

285 driven currents also result in a downwind upwelling, despite both of the wind-driven currents and upwelling of the winter observation are weaker than those of the summer observation (Fig. 10). These summer and winter upwelling processes provided us excellent chance to evaluate the performance of the WCCM in Lake Taihu.

The numerical solutions of the governing equations and most parameter values of the WCCM are similar to those of the EFDC. The main differences between the two models are the vertical eddy viscosity, the wind drag coefficient, and the

290 wave-induced radiation stress. The numerical experiments shows that the average correlation coefficient between the WCCM-simulated and measured current speeds increased by 36.4% compared with the results of the LCM_1, or 42.9% compared with the results of the EFDC in 2018. The current direction and field simulated by the WCCM are also improved,

whereas the water level is simulated at similar accuracy as by the EFDC. The WCCM can accurately simulate the wind-driven currents, and subsequent the downwind upwelling in Lake Taihu.

5.1 Wind drag coefficient

This variable is a key parameter for hydrodynamic numerical models. The EFDC parameter sensitivity analysis shows that the wind drag coefficient is the most sensitive parameter for simulating current velocity in Lake Taihu (Li et al., 2015). The correlation coefficients between the simulated and measured current speeds of LCM_2 and WCCM, which use the new expression of C_s, considering the discontinuity of changing trend and directionality of wind momentum transmission, are significantly greater than those of EFDC and LCM_1 (Tables 3 and 5). This implies that the use of the new C_s mainly contributes to the increase of the correlation coefficient.

A piecewise function is firstly proposed in this study to describe the discontinuity of the changing trend of the wind momentum transmission. The changing trend of the wind drag coefficient at the water surface is discontinuous (Wu, 1980). The atmospheric surface layer appears to be aerodynamically rough related to wind waves for wind speeds > 7.5 m s^{-1} and aerodynamically smooth for wind speeds < 3 m s^{-1} (Wu, 1980). The transmission efficiency of wind momentum to the water under aerodynamically rough conditions is higher than that under aerodynamically smooth conditions (Lükő et al., 2020). Field observations of Lake Taihu indicate that C_s increases with wind speed (Xiao et al., 2013). A critical wind speed of 7.5 m s^{-1} is therefore adopted to describe the discontinuity. As shown in Eqs. (8) and (9), a logistic curve is used to describe the increase of C_s for wind speeds > 7.5 m s^{-1}, otherwise C_s is a constant value.

The directionality of wind momentum transmission is further addressed using different C_s values in the *x*- and *y*-directions. There have been numerous expressions designed to calculate wind drag coefficient based on ocean environments (Geernaert et al., 1987; Large and Pond, 1981; Lükő et al., 2020; Wu, 1980; Zhou et al., 2009). However, few expressions consider the directionality of wind momentum transmission. There is a contradiction that: C_s increases with wind speed (Lükő et al., 2020; Xiao et al., 2013), while the tilt of water surface along wind direction in large shallow lakes with limited water depth and fetch due to the upwelling will decrease the wind momentum transmission efficiency. Because of this contradiction, the same transmission efficiency of wind momentum is used in both of being perpendicular and parallel to wind directions, which may over- or under-estimate the wind drag coefficient in any one direction.

5.2 Wave-induced radiation stress

This is the first time for wave-induced radiation stress to be considered in simulating wind-driven currents in large shallow lakes. The results show that it can improve the simulated current direction. In 2015, the MAE_{UVD} values of the LCM_2 (average MAE_{UVD} of 56.3 °; Table 3) are greater than those of the WCCM (average MAE_{UVD} of 52.9 °; Table 4). A similar result can be achieved by comparing the MAE_{UVD} values between the LCM_2 and WCCM in 2018 (Table 5). Moreover, the correlation coefficients of LCM_2 in 2018 are slightly less than those of the WCCM in 2018 (Table 5), which implies that wave-induced radiation stress can also contribute to the improvement of the WCCM-simulated current speed.

325   The comparison between the WCCM- and EFDC-simulated current fields further demonstrates the importance of wave-induced radiation stress. Although the current field simulated by the WCCM is similar to that by the EFDC, the vortex locations simulated by these models are quite different. In 2015, the middle and bottom current fields simulated by the EFDC exhibit counterclockwise vortexes in Zhushan Bay and Meiliang Bay (Fig. B.1), which are located in the downwind area, but the current fields simulated by the WCCM do not show the same phenomenon. This is because the interaction

330   between wind waves and lake currents in the downwind area is violent owing to wave deformation resulting from the shallow water and lakeshore. The wave-induced radiation stress makes the vortex less likely to form in this area. Conversely, the middle and bottom current fields simulated by the LCM_2 without wave-induced radiation stress also show counterclockwise vortexes in Zhushan Bay and Meiliang Bay (Fig. B.3), which is similar to the result of the EFDC.

5.3 Vertical eddy viscosity

335   Comparing with other variables, the vertical eddy viscosity play a less prominent part in the development of the wind-driven currents. In our study, Mellor-Yamada level-2.5 turbulence closure model (Mellor and Yamada, 1982; Ji et al., 2001) is adopted in the EFDC and the other parameters are determined after parametric uncertainty and sensitivity analysis (Li et al., 2015), while a simple turbulence scheme (equation (4)-(6)) is adopted in the LCM_1. However, the accuracy of the LCM_1 is rather similar to that of the EFDC (Tables 2, 3, 4, and 5), which implies that the high-order turbulence scheme does not

340   improve the lake current simulations (Koue et al. 2018), while the simple turbulence scheme makes the WCCM more efficient.

6 Conclusion

The strong summer or winter winds generate wind-driven currents in Lake Taihu, and subsequent results in downwind upwelling. Based these processes and numerical experiments, a wave-current coupled model (WCCM) is developed by

345   reconsidering the expressions of winds, wind waves, and turbulence. It can accurately simulate the development of wind-driven currents with a 42.9% increase of simulated current speed compared with the EFDC results of 2018. The new expression of the wind drag coefficient is mainly responsible to increase of the correlation coefficient between the WCCM-simulated and measured current speeds. The introduction of wave-induced radiation stress can contribute to the improvement of the simulated current direction and fields, and slightly improve the simulation of current speed. Moreover, the simple

350   parameterized turbulence scheme is sufficient for the simulation of wind-driven currents in Lake Taihu.

It should be noted that despite the performance of the numerical models had been greatly improved, the correlation between simulated and measured current speed remains low, especially for the 2018 observation. Actually, few model studies are reported to conduct this correlation analysis because of lack data or worse results. Therefore, we urge that more process-based field observations are required to help us to fully understand the real hydrodynamic characteristics of large shallow

355   lakes and further improve the performance of shallow lake current models.

Code and data availability

The source code of the EFDC model is freely available from https://github.com/dsi-llc/EFDCPlus. The software named EFDC_Explorer 8.3 was purchased from DSI LLC (https://www.eemodelingsystem.com/). The configurations, inputs and outputs of the EFDC model for all simulated episodes are available from https://doi.org/10.5281/zenodo.5180640 (Wu, 360 2021).

The source code of the SWAN model is freely available from http://swanmodel.sourceforge.net/.

The source code of the WCCM model is available from https://doi.org/10.5281/zenodo.5181451 (Wu and Qin, 2021) with restricted access because of the copyright protection. The access of the source code of the WCCM model is granted by first author or corresponding author. Alternatively, a frozen version of the code of the WCCM model with the configurations, 365 inputs and outputs of the model as used in this paper is freely archived from https://doi.org/10.5281/zenodo.5181754 (Wu and Qin, 2021).

The dataset of measured water level and current is available from https://doi.org/10.5281/zenodo.5184459 (Hu and Wu, 2021) with restricted access. The access of the dataset is granted by first author or corresponding author. The other datasets used in this paper are included in the simulated episodes on zenodo (e.g. https://doi.org/10.5281/zenodo.5180640).

370 **Author contributions**

Tingfeng Wu and Boqiang Qin participated in the conceptualization, design, definition of intellectual content, literature search, model development, data acquisition and analysis, and manuscript preparation. Anning Huang, Yongwei Sheng, and Céline Casenave assisted with the model evaluation and manuscript editing. Anning Huang, and Shunxin Feng collected significant background information and assisted with data acquisition, data analysis and statistical analysis.

375 **Compliance with ethical standards**

Conflict of interest

The authors declare that they have no conflict of interest.

Ethical approval and consent to participate

Not applicable.

Consent for publication

 Not applicable.

References

Ardhuin, F., Jenkins, A. D., and Belibassakis, K. A.: Comments on "The three-dimensional current and surface wave equations", J. Phys. Oceanogr., 38(6), 1340-50, 2008.

Blumberg, A. F., and Mellor, G. L.: A description of a three-dimensional coastal ocean circulation model, In: Heaps, N. (eds.): Three-dimensional Coastal Ocean Models, pp. 1-16, 1987.

Booij, N., Ris, R. C., and Holthuijsen, L. H.: A third-generation wave model for coastal regions, Part I, Model description and validation, J. Geophys. Res.-Oceans, 104(C4), 7649-7666, 1999.

Booij, N., Haagsma, I. J. G., Holthuijsen, L. H., Kieftenburg, A. T. M. M., Ris, R. C., van der Westhuysen, A. J., and Zijlema, M.: SWAN Cycle III version 40.41 Use Manual, Delft University of Technology, 2600 GA DELFT, The Netherlands, http://fluidmechanics.tudelft.nl/swan/index.htm, 2004.

Butler, H. L.: Evolution of a Numerical Model for Simulating Long-Period Wave Behavior in Ocean-Estuarine Systems, In: Hamilton, P., Macdonald, K.B. (eds.): Estuarine and Wetland Processes, Marine Science, 11, Springer, Boston, MA, https://doi.org/10.1007/978-1-4757-5177-2_6, 1980.

Carvalho, D., Rocha, A., Gómez-Gesteira, M., and Santos, C.: A sensitivity study of the WRF model in wind simulation for an area of high wind energy, Environ. Modell. Softw., 33(7), 23-34, 2012.

Chen, C., Huang, H., Beardsley, R. C., Xu, Q., Limeburner, R., Cowles, G. W., Sun, Y., Qi, J., and Lin, H.: Tidal dynamics in the Gulf of Maine and New England Shelf: An application of FVCOM, J. Geophys. Res., 116, C12010, 2011.

Chen, F., Zhang, C., Brett, M. T., and Nielsen, J. M.: The importance of the wind-drag coefficient parameterization for hydrodynamic modeling of a large shallow lake, Ecol. Inform., 101106, 2020.

Coastal Engineering Research Center: Shore protection manual, U.S. Army Coastal Engineering Center, 1984.

Feng, T., Wang, C., Wang, P., Qian, J., and Wang, X.: How physiological and physical processes contribute to the phenology of cyanobacterial blooms in large shallow lakes: a new Euler-Lagrangian coupled model, Water Res., 140(1), 34-43, 2018.

410 Geernaert, G. L., Larssen, S. E., and Hansen, F.: Measurements of the wind-stress, heat flux, and turbulence intensity during storm conditions over the North Sea, J. Geophys. Res.-Oceans, 98, 16571-16582, 1987.

Hamrick, J. M., 1992. A Three-Dimensional Environmental Fluid Dynamics Computer Code: Theoretical and Computational Aspects, Special Report No. 317 in Applied Marine Science and Ocean Engineering, College of William and 415 Mary, Virginia Institute of Marine Science, 1992.

Han, Y., Fang, H., Huang, L., Li, S., and He, G.: Simulating the distribution of *Corbicula fluminea* in Lake Taihu by benthic invertebrate biomass dynamic model (BIBDM), Ecol. Model., 409, 108730, 2019.

Hofmann, H., Lorke, A., and Peeters, F.: The relative importance of wind and ship waves in the littoral zone of a large lake, Limnol. Oceanogr., 53, 368-380, 2008.

420 Huang, A., Rao, Y. R., Lu, Y., and Zhao, J.: Hydrodynamic modeling of Lake Ontario: An intercomparison of three models, J. Geophys. Res.-Oceans, 115, C12076, doi:10.1029/2010JC006269, 2010.

Hutter, K., Wang, Y., and Chubarenko, I. P.: Physics of lakes. Volume 1: foundation of the mathematical and physical background, Springer, 2011.

Jeffreys, H.: On the formation of wave by wind, P. Roy. Soc. A, 107(742), 189-206, 1925.

425 Ji, C., Zhang, Q., and Wu, Y.: Derivation of three-dimensional radiation stress based on Lagrangian solutions of progressive waves, J. Phys. Oceanogr., doi: https://doi.org/10.1175/JPO-D-16-0277.1, 2017.

Jin, K. R., Hamrick, J. H., and Tisdale T.: Application of three-dimensional model for Lake Okeechobee, J. Hydraul. Eng., 126, 758-771, 2000.

Jin, K. R., and Ji, Z. G.: Application and validation of three-dimensional model in a shallow lake, J. Waterw. Port Coast., 430 Ocean Eng., 131, 213-225, 2005.

Ji, Z. G.: Hydrodynamics and Water Quality: Modeling Rivers, Lakes, and Estuaries, John Wiley and Sons, Inc., Hoboken, New Jersey, USA, 2008.

Ji, Z. G., Morton, M. R., and Hamrick, J. M.: Wetting and drying simulation of estuarine processes, Estuar. Coast. Shelf S., 53(5), 683-700, 2001.

435 Koue, J., Shimadera, H., Matsuo, T., and Kondo, A.: Evaluation of thermal stratification and flow field reproduced by a three-dimensional hydrodynamic model in Lake Biwa, Japan, Water, 10, 47, doi: http://dx.doi.org/10.3390/w10010047, 2018.

Kumar, N., Voulgaris, G., and Warner, J. C.: Implementation and modification of a three-dimensional radiation stress formulation for surf zone and rip-current applications, Coast. Eng., 58(12), 1097-1117, 2011.

440 Large, W. G, Pond, S.: Open ocean momentum flux measurements in moderate to strong winds, J. Phys. Oceanogr., 11, 324-336, 1981.

15

Longuet-Higgins, M. S., and Stewart, R. W.: Radiation stresses in water waves: a physical discussion, with application, Deep-Sea Res., 11(4): 529-562, 1964.

Li, Y., Acharya, K., and Yu, Z.: Modeling impacts of Yangtze River water transfer on water ages in Lake Taihu, China, Ecol.

445   Eng., 37, 325–334, 2011.

Li, Y., Pang, Y., and Liu, X.: Study on the influence mechanism about current to wave in Lake Taihu. J. Hydraul. Eng., 38(Supplement), 303-308, 2007. (in Chinese with English abstract)

Li, Y., Tang, C., Zhu, J., Pan, B., Anim, D. O., Ji, Y., Yu, Z., and Acharya, K.: Parametric uncertainty and sensitivity analysis of hydrodynamic processes for a large shallow freshwater lake, Hydrolog. Sci. J., 60 (6), 1078-1095, 2015.

450   Lükő, G., Torma, P., Krámer, T., Weidinger. T., Vecenaj, Z., and Grisogono, B.: Observation of wave-driven air-water turbulent momentum exchange in a large but fetch-limited shallow lake, Adv. Sci. Res., 17, 175-182, 2020.

MacIntyre, S., Bastviken, D., Arneborg, L., Crowe, A. T., Karlsson, J., Andersson A., Gålfalk, M., Rutgersson, Anna., Podgrajsek, E., and Melack, J. M.: Turbulence in a small boreal lake: Consequences for air-water gas exchange, Limnol. Oceanogr., 9999, 1-28, doi: 10.1002/lno.11645, 2020.

455   Mellor, G. L.: The depth-dependent current and wave interaction equations: a revision, J. Phys. Oceanogr., 38(11), 2587-2596, 2008.

Mellor, G.L. and Yamada, T.: Development of a turbulence closure model for geophysical fluid problems, Rev. Geophys. Space Phys., 20(4), 851-875, 1982.

Morey, S. L., Gopalakrishnan, G., Sanz E. P., De Souza, J. M. A. C., Donohue, K., Pérez-Brunius, P., Dukhovskoy, D.,

460   Chassignet, E., Cornuelle, B., Bower, A., Furey, H., Hamilton, P., and Candela J.: Assessment of numerical simulations of deep circulation and variability in the Gulf of Mexico using recent observations, J. Phys. Oceanogr., 50(4), 1045-1064, 2020.

Munk, W. H.: Wind stress on water: an hypothesis, Q. Roy. Meteor. Soc., 320-332, 1955.

Rey, A., Mulligan, R., Filion, Y., da Silva, A. M., Champagne, P. and Boegman, L.: Three-dimensional hydrodynamic behaviour of an operational wastewater stabilization pond, J. Environ. Eng. ASCE, 147(2), 05020009, doi:

465   10.1061/(ASCE)EE.1943-7870.0001834, 2021.

Schoen, J. H., Stretch, D. D., and Tirok, K.: Wind-driven circulation patterns in a shallow estuarine lake: St Lucia, South Africa, Estuar. Coast. Shelf S., 146, 49-59, 2014.

Shchepetkin, A. F., and McWilliams, J. C.: The regional oceanic modeling system (ROMS): a split-explicit, free-surface, topography-following-coordinate oceanic model, Ocean Model., 9(4), 347-404,2005.

470   Sterner, R. W., Ostrom, P., Ostrom, N. E., Klump, J. V., Steinman, A. D., Dreelin, E. A., Zanden, M. J. V., and Fisk, A. T.: Grand challenges for research in the Laurentian Great Lakes, Limnol. Oceanogr., 62, 2510–2523, 2017.

Sun, F., Wei, Y., and Wu, K.: Wave-induced radiation stress under geostrophic condition. Acta Oceanologia Sinica, 28(6), 1-4, 2006. (in Chinese with English abstract)

Vinçon-Leite, B., and Casenave, C.: Modelling eutrophication in lake ecosystems: A review, Sci. Total Environ., 651, 2985–

475   3001, 2019.

Wang, Z., Wu, T., Zou, H., Jia, X., Huang, L., Liang, C., and Zhang, Z.: Changes in seasonal characteristics of wind and wave in different regions of Lake Taihu, J. Lake Sci., 28(1), 217-224, 2016. (in Chinese with English abstract)

Wang, C., Shen, C., Wang, P. F., Qian, J., Hou, J., and Liu, J. J.: Modeling of sediment and heavy metal transport in Taihu Lake, China, J. Hydrodyn. Ser. B, 25(3), 379-387, 2013.

480 Warner, J. C., Sherwood, C. R., Signell, R. P., Harris, C. K., and Arango, H. G.: Development of a three-dimensional, regional, coupled wave, current, and sediment-transport model, Comput. Geosci., 34(10): 1284-1306, 2008.

Wei, Z., Miyano, A., and Sugita, M.: Drag and bulk transfer coefficients over water surfaces in light winds, Bound.-Lay. Meteorol., 160 (2), 319-346, 2016.

Wu, J.: Wind-stress coefficients over sea surface near neutral conditions-A revisit, J. Phys. Oceanogr., 10(5), 727-740, 1980.

485 Wu, L., Chen, C, Guo, P, Shi, M, Qi, J., and Ge, J.: A FVCOM-based unstructured grid wave, current, sediment transport model, I. model description and validation, J. Ocean U. China, 10 (1), 1-8, 2011.

Wu, T., Qin, B., Brookes, J. D., Yan, W., Ji, X., Feng, J., Ding, W., and Wang, H.: Spatial distribution of sediment nitrogen and phosphorus in Lake Taihu from a hydrodynamics-induced transport perspective, Sci. Total Environ., 650, 1554-1565, 2019.

490 Wu, T., Qin, B., Ding, W., Zhu, G., Zhang, Y., Gao, G., Xu, H., Li, W., Dong, B., and Luo, L.: Field observation of different wind-induced basin-scale current field dynamics in a large, polymictic, eutrophic lake, J. Geophys. Res.-Oceans, 123, 6945–6961, 2018.

Wüest, A., and Lorke, A.: Small-scale hydrodynamics in lakes. Annu. Rev. Fluid Mech., 35, 373-412, 2003.

Xiao, W., Liu, S., Wang, W., Yang, D., Xu, J., Cao, C., Li, H., and Lee, X.: Transfer coefficients of momentum, heat and 495 water vapour in the atmospheric surface layer of a large freshwater lake. Bound.-Lay. Meteorol., 148, 479-494, doi: 10.1007/s10546-013-9827-9, 2013.

Xu, X., Tao, R., Zhao, Q., and Wu, T.: Wave characteristics and sensitivity analysis of wind field in a large shallow lake-Lake Taihu, J. Lake Sci., 25(1), 55-64, 2013. (in Chinese with English abstract)

Xu, Z. G., and Bowen, A. J.: Wave- and wind-driven flow in water of finite depth, J. Phys. Oceanogr., 24, 1850-1866, 1994.

500 Zhao, Q., Sun, J., and Zhu, G.: Simulation and exploration of the mechanisms underlying the spatiotemporal distribution of surface mixed layer depth in a large shallow lake, Adv. Atmos. Sci., 29(6), 1360-1373, doi: 10.1007/s00376-012-1262-1, 2012.

Zhou, J., Zeng, C., and Wang, L.: Influence of wind drag coefficient on wind-driven flow simulation, Chinese J. Hydrodyn., 24(4), 440-447, 2009. (In Chinese with English abstract)

505 Zhou, L., Chen, D., Karnauskas, K. B., Wang, C., Lei, X., Wang, W., Wang, G., and Han, G.: Introduction to special section on oceanic responses and feedbacks to tropical cyclones, J. Geophys. Res.-Oceans, 123, 742–745. Doi: 10.1002/2018JC013809

510 **Table 1 Parameter values and variable equations used for lake current simulation in the LCM**

Parameter	Description	Value	Unit
φ	Latitude	31.245	°
g	Gravitational acceleration	9.8	$m\ s^{-2}$
A_H	Horizontal eddy viscosity	1	$m^2\ s^{-1}$
A_v	Vertical eddy viscosity	Equation(4),(5) and (6)	$m^2\ s^{-1}$
z_0	Roughness height of lakebed	0.005	m
r_s	Roughness of lake surface	0.01	
κ	von Kármán constant	0.4	
ρ_a	Air density	1.293	$kg\ m^{-3}$
C_s	Wind drag coefficient	Equation(8) and (9)	
C_B	Drag coefficient of lakebed	Equation(11)	

515

520

525

530

Table 2 Correlation coefficient (*r*) and mean absolute error ($RMSE_{\mathrm{WL}}$) between the simulated and measured water level during 2015 observation for the numerical experiments

Model	Statistics	WL1	WL2	WL3	WL4	WL5
EFDC	*r*	0.96[**]	0.95[**]	0.66[**]	0.89[**]	0.89[**]
	RMSE	0.05	0.05	0.05	0.05	0.06
LCM_1	*r*	0.96[**]	0.95[**]	0.72[**]	0.89[**]	0.90[**]
	RMSE	0.05	0.05	0.04	0.05	0.06
LCM_2	*r*	0.96[**]	0.95[**]	0.62[**]	0.92[**]	0.83[**]
	RMSE	0.04	0.04	0.04	0.05	0.06
WCCM	*r*	0.96[**]	0.94[**]	0.66[**]	0.90[**]	0.84[**]
	RMSE	0.03	0.04	0.04	0.05	0.06

535 *p < 0.05, **p < 0.01.

540

545

550

555

Table 3 Correlation coefficient (*r*) and mean absolute error between the simulated and measured current velocity (current speed, *MAE*_{UV}; current direction, *MAE*_{UVD}) during the 2015 observation for the numerical experiments

Model	Surface			Middle			Bottom		
	r	MAE_{UV} (m s^{-1})	MAE_{UVD} (°)	r	MAE_{UV} (m s^{-1})	MAE_{UVD} (°)	r	MAE_{UV} (m s^{-1})	MAE_{UVD} (°)
EFDC	0.44[**]	0.023	60.8	0.49[**]	0.020	55.2	0.45[**]	0.021	55.0
LCM_1	0.58[**]	0.026	62.6	0.60[**]	0.025	54.1	0.53[**]	0.025	54.5
LCM_2	0.63[**]	0.023	56.7	0.65[**]	0.026	55.5	0.55[**]	0.026	56.7
WCCM	0.64[**]	0.024	58.2	0.70[**]	0.023	48.6	0.64[**]	0.021	52.1

*$p < 0.05$, **$p < 0.01$.

560

565

570

575

580

20

Table 4 Correlation coefficient (r) and mean absolute error ($RMSE$) between the simulated and measured water level during the 2018 observation for the numerical experiments

Model	Statistics	WL1	WL2	WL3	WL4	WL5
EFDC	r	0.91[**]	0.95[**]	0.80[**]	0.82[**]	0.88[**]
	$RMSE$	0.04	0.03	0.05	0.03	0.07
LCM_1	r	0.91[**]	0.95[**]	0.79[**]	0.84[**]	0.89[**]
	$RMSE$	0.05	0.04	0.06	0.03	0.08
LCM_2	r	0.91[**]	0.95[**]	0.81[**]	0.84[**]	0.89[**]
	$RMSE$	0.03	0.02	0.05	0.02	0.05
WCCM	r	0.91[**]	0.94[**]	0.81[**]	0.82[**]	0.89[**]
	$RMSE$	0.02	0.02	0.05	0.02	0.06

585 $*P < 0.05, **P < 0.01.$

590

595

600

605

Table 5 Correlation coefficient (*r*) and mean absolute error between the simulated and measured current velocity (current speed, *MAE*$_{UV}$; current direction, *MAE*$_{UVD}$) during the 2018 observation, for the numerical experiments

Model	Surface			Middle			Bottom		
	r	*MAE*$_{UV}$ (m s^{-1})	*MAE*$_{UVD}$ (°)	*r*	*MAE*$_{UV}$ (m s^{-1})	*MAE*$_{UVD}$ (°)	*r*	*MAE*$_{UV}$ (m s^{-1})	*MAE*$_{UVD}$ (°)
EFDC	0.29[**]	0.021	81.4	0.19[**]	0.019	77.2	0.15[*]	0.021	72.4
LCM_1	0.28[**]	0.020	83.6	0.22[**]	0.021	74.5	0.16[*]	0.023	73.5
LCM_2	0.32[**]	0.020	83.8	0.29[**]	0.019	74.4	0.26[*]	0.021	72.8
WCCM	0.31[**]	0.020	81.2	0.31[**]	0.019	73.5	0.28[**]	0.021	72.4

*$P < 0.05$, **$P < 0.01$.

610

615

620

625

630
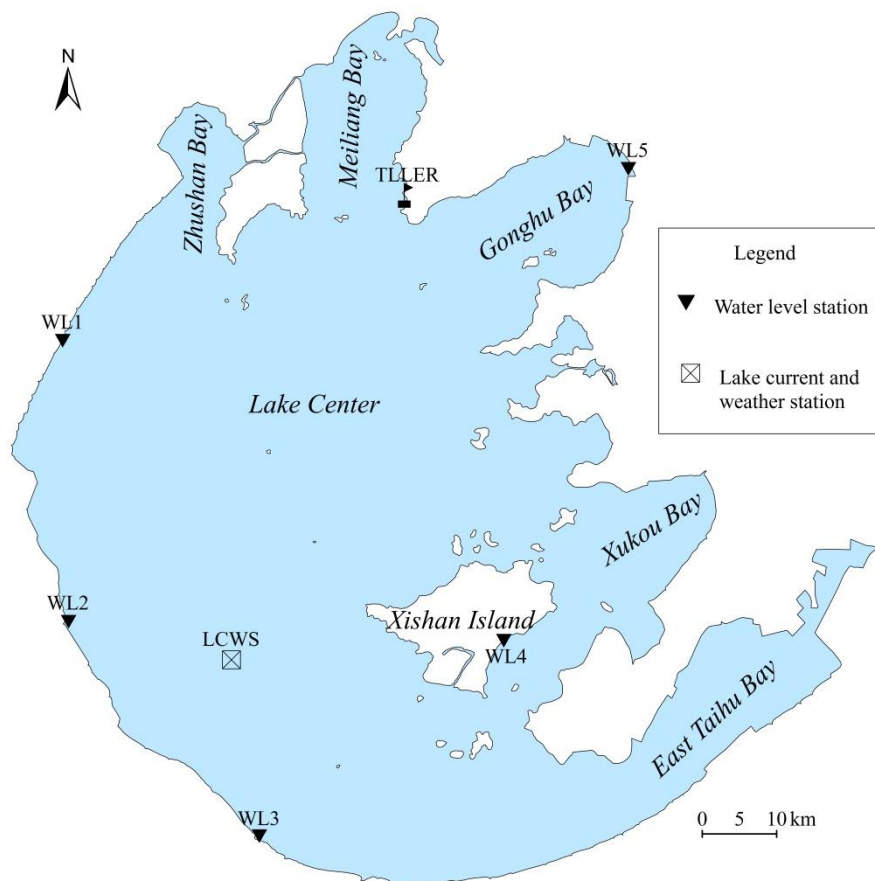
Figure 1: Location of the Taihu Laboratory for Lake Ecosystem Research (TLLER), the five water level stations (WL1–WL5), and the Lake Current and Weather Station (LCWS) for recording the lake currents and meteorological data.

640
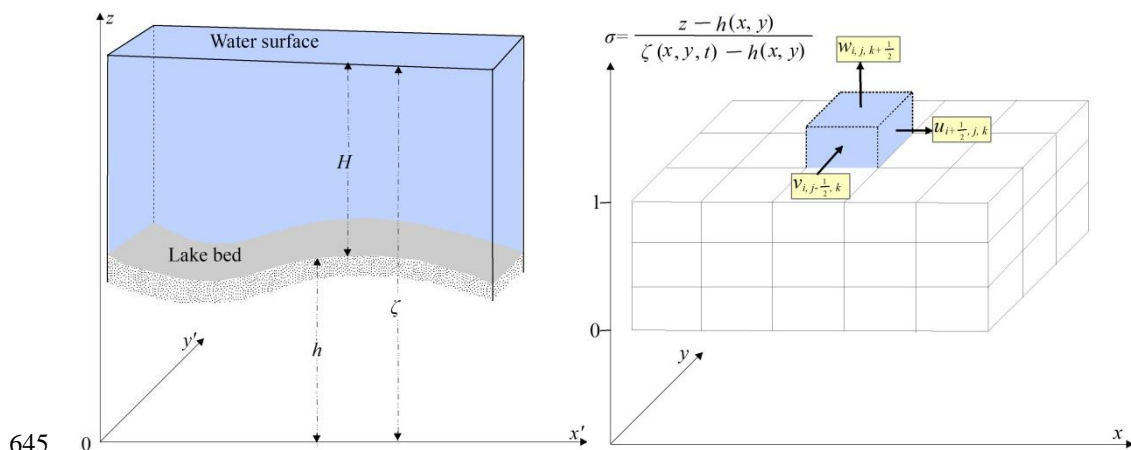
Figure 2: Lake bed elevation (h), water level (ζ), and water depth (H) in the Cartesian coordinate system (left). The three components of lake current velocity in the ith (x-direction), j^{th} (y-direction), and k^{th} (σ-direction) grid of the mesh in the sigma (σ) coordinate system (right).

Figure 3: Structure of the Wave-Current Coupled Model (WCCM) obtained by two-way coupling SWAN and LCM models, with the variables definition and the data transmission between the meshes.

665

670
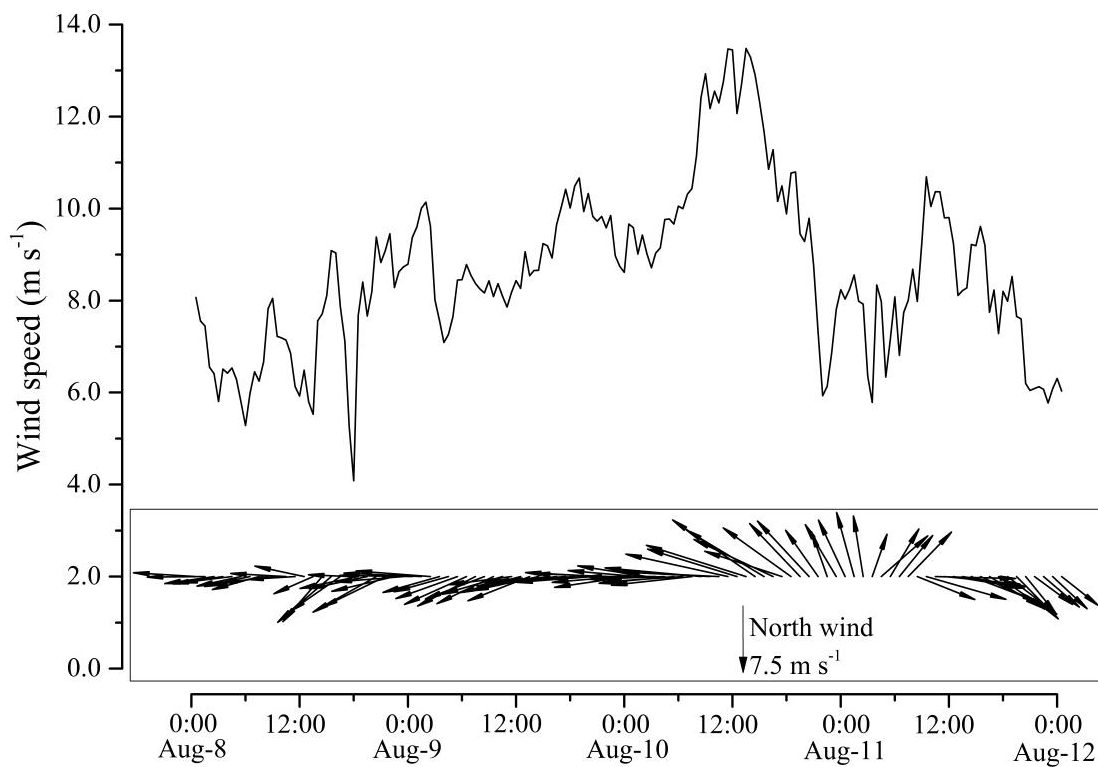
Figure 4: Variation of wind speed and wind direction at 10 m above the water surface at the LCWS station during the 2015 observation.

675

680

685
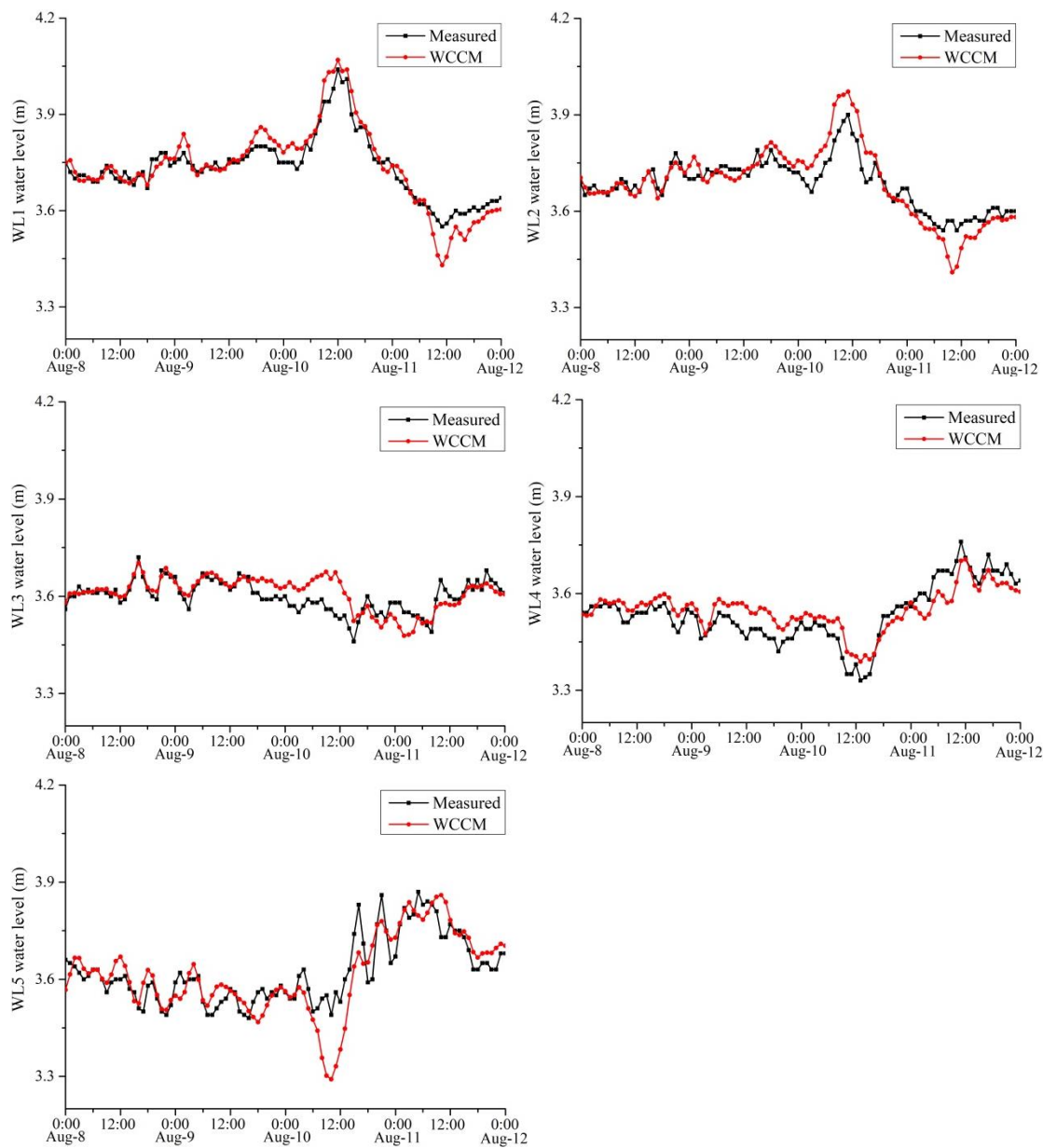
Figure 5: Comparison between the WCCM-simulated and measured water levels at the WL1–WL5 stations during the 2015 observation.
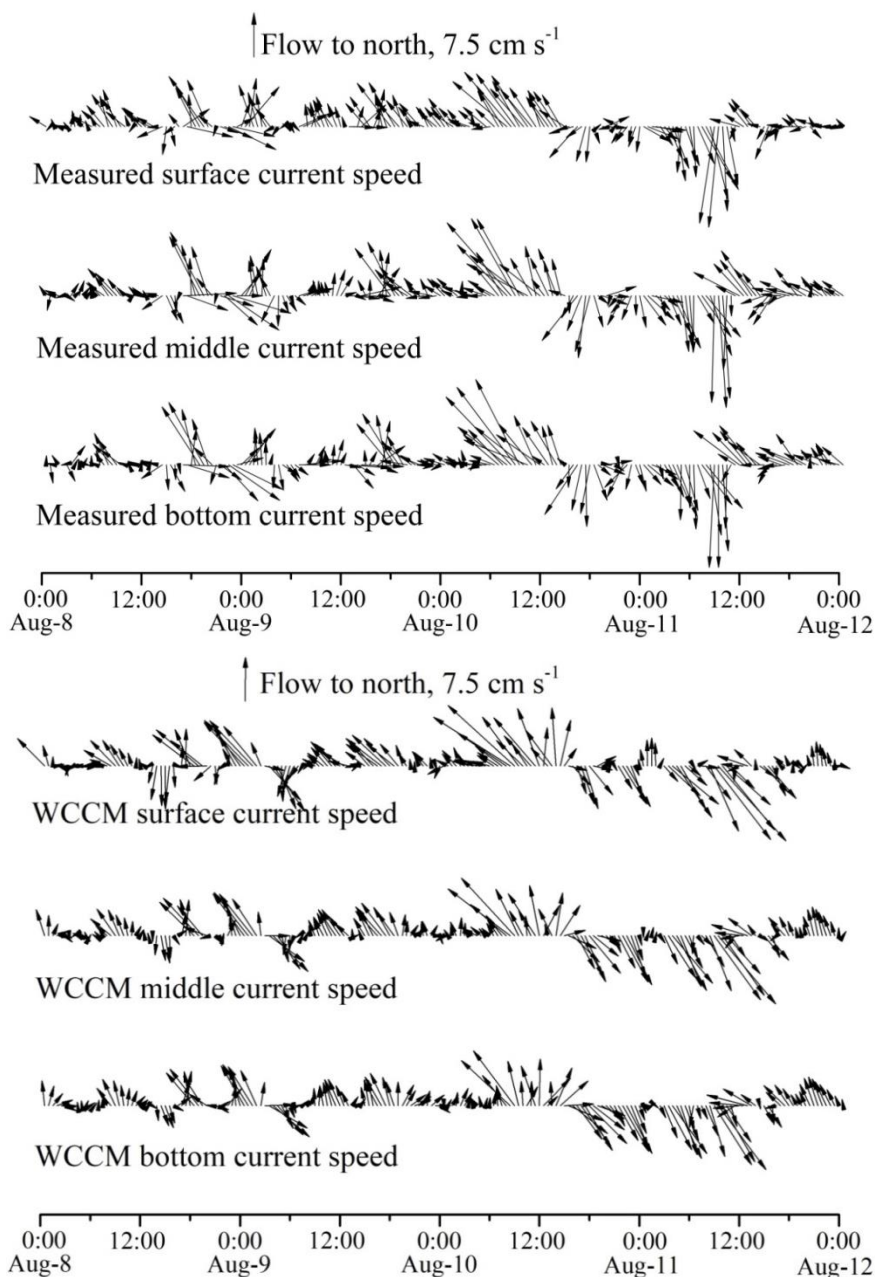
Figure 6: Comparison between the measured and WCCM-simulated current speeds in the lake surface, middle, and bottom water layer at the LCWS station during the 2015 observation.

WCCM Surface current field

EFDC Surface current field

WCCM Middle current field

EFDC Middle current field

WCCM Bottom current field

EFDC Bottom current field
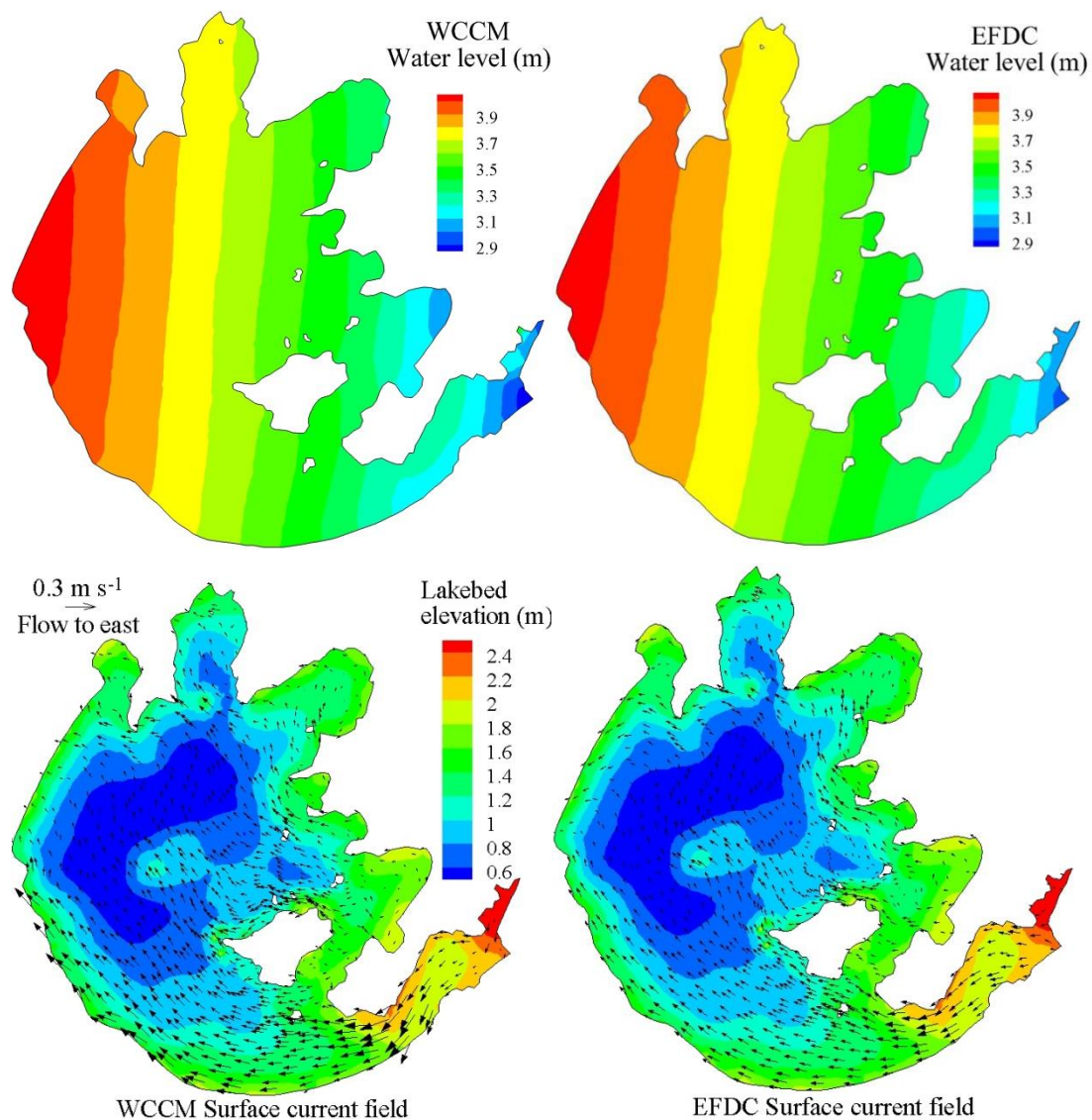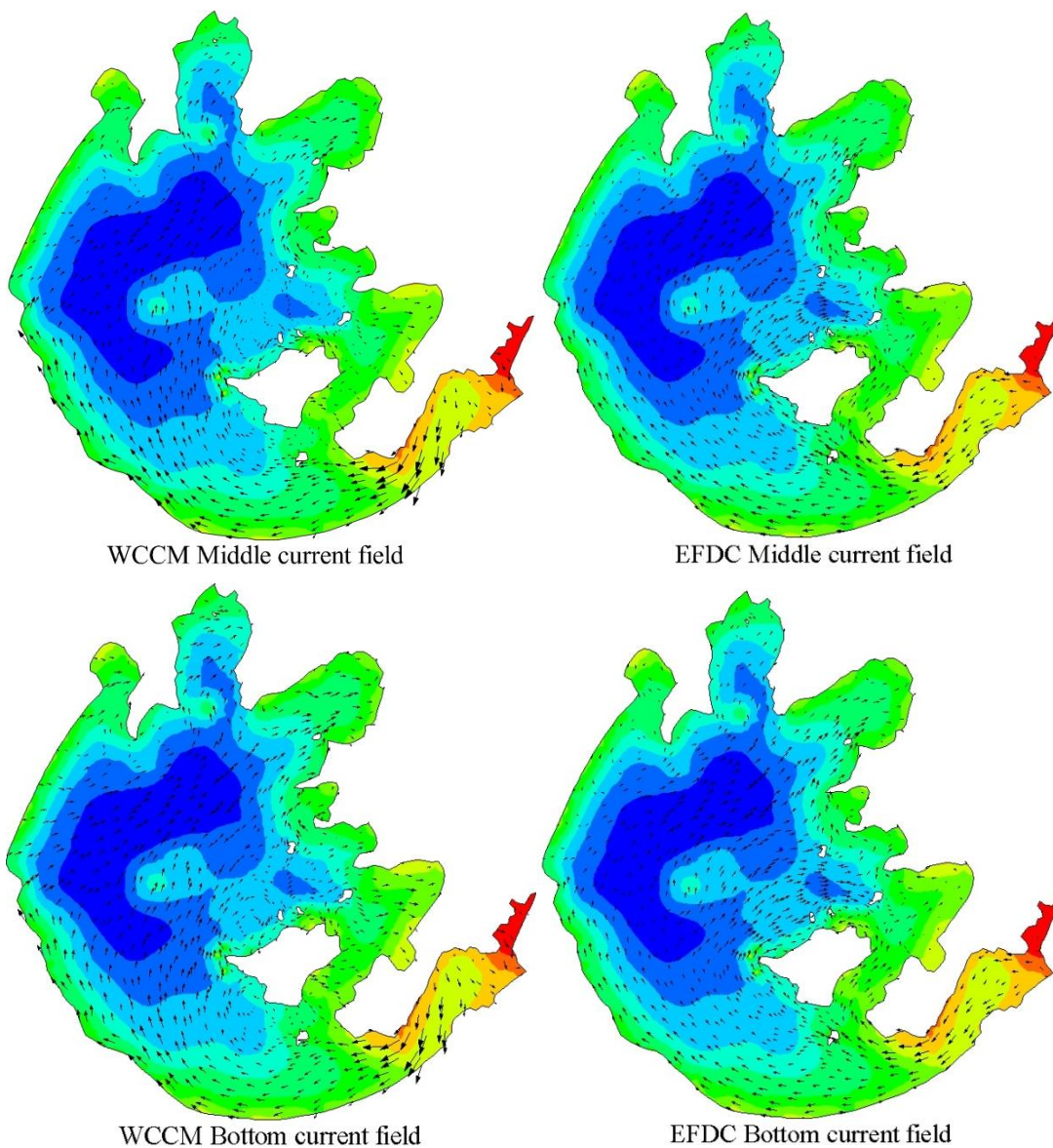
Figure 7: Comparison of the contour of water level and current fields in the surface, middle, and bottom water layers simulated by the WCCM with those simulated by the EFDC at 13:00 on August 10, 2015.

705

710
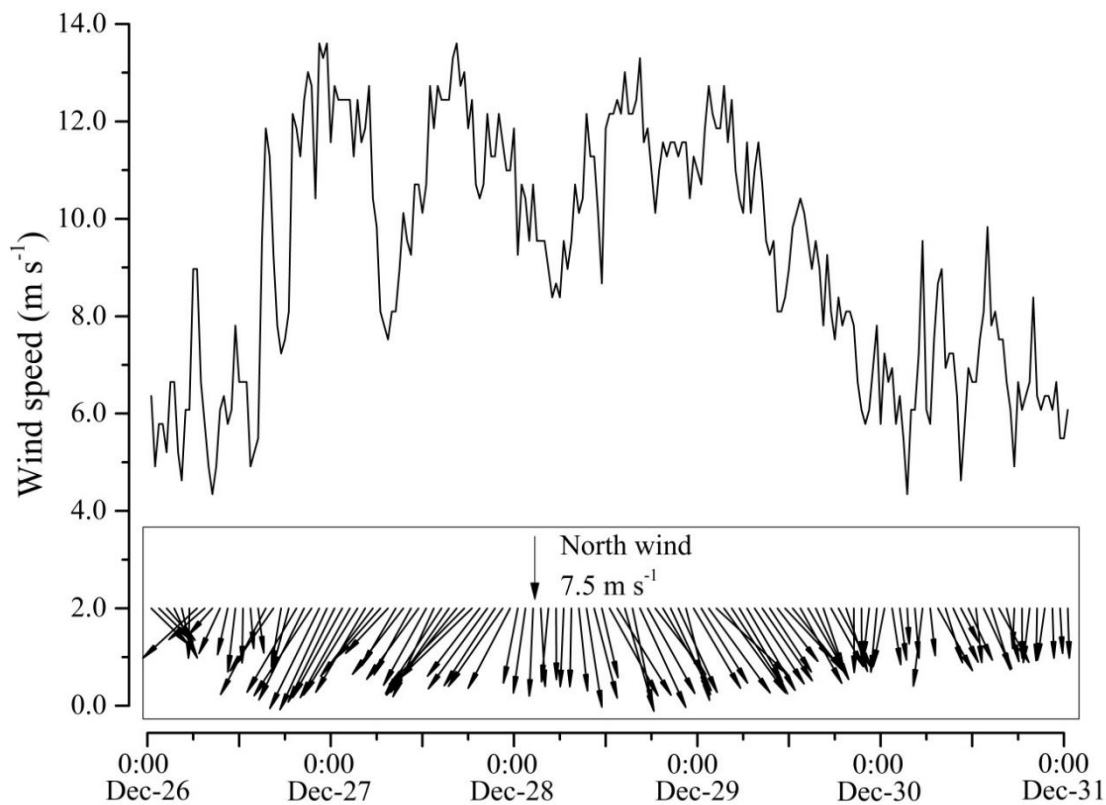
Figure 8: Variation of wind speed and direction at 10 m above the water surface at the LCWS station during the 2018 observation.
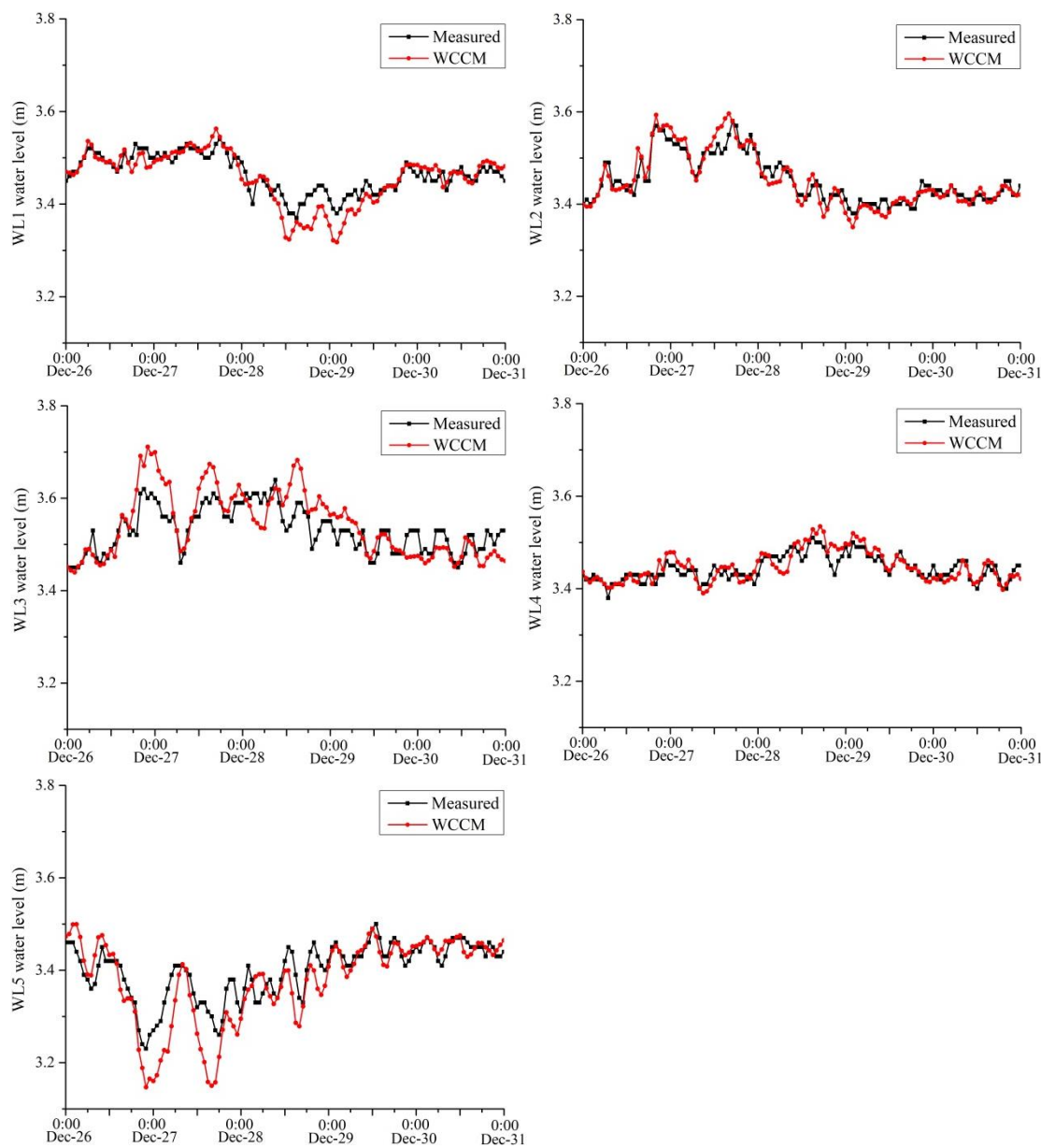
Figure 9: Comparison between the WCCM-simulated and measured water levels at the WL1–WL5 stations during the 2018
730 **observation.**
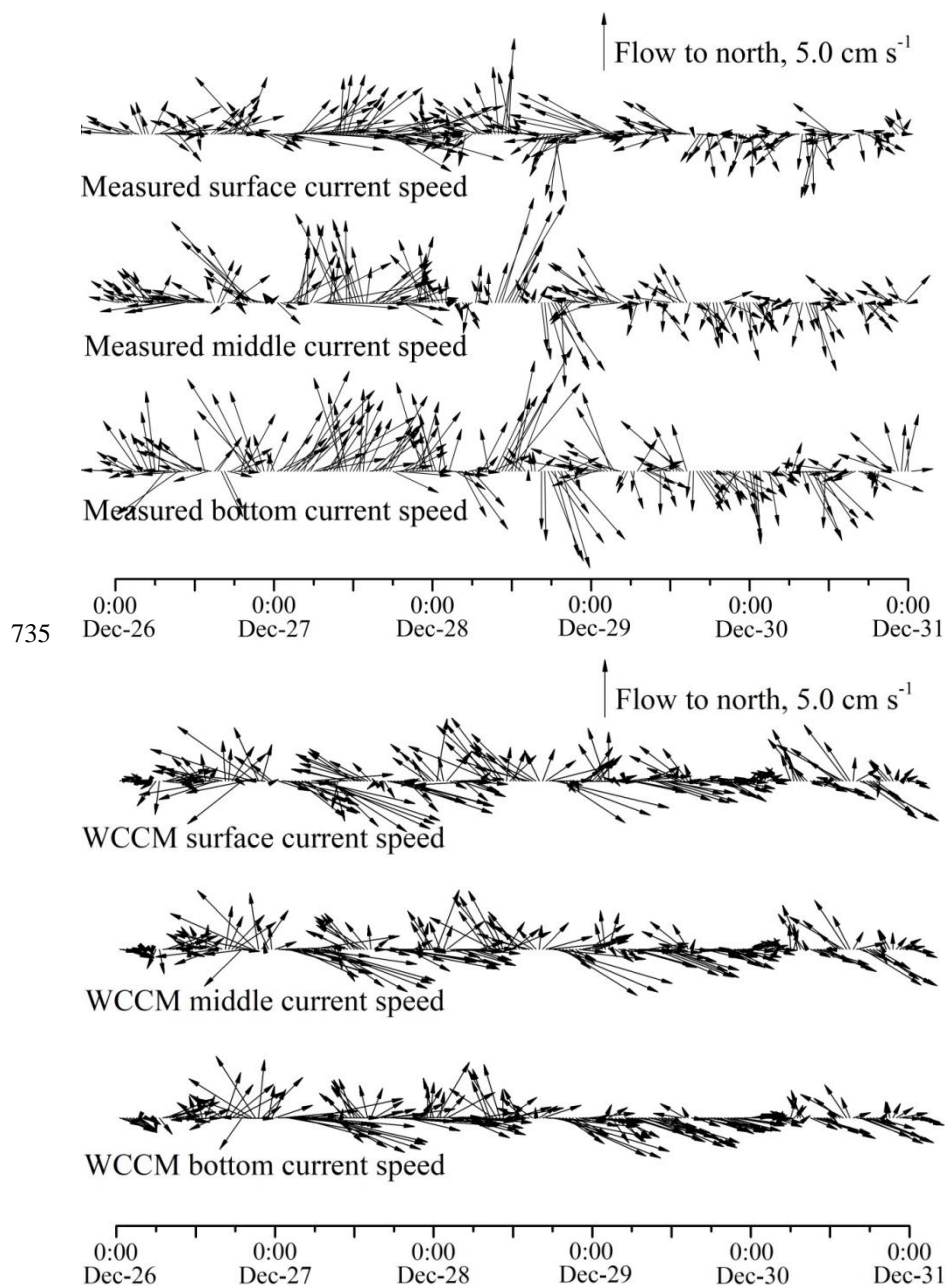
Figure 10: Comparison between the measured and WCCM-simulated surface, middle, or bottom current speeds at the LCWS station during the 2018 observation.
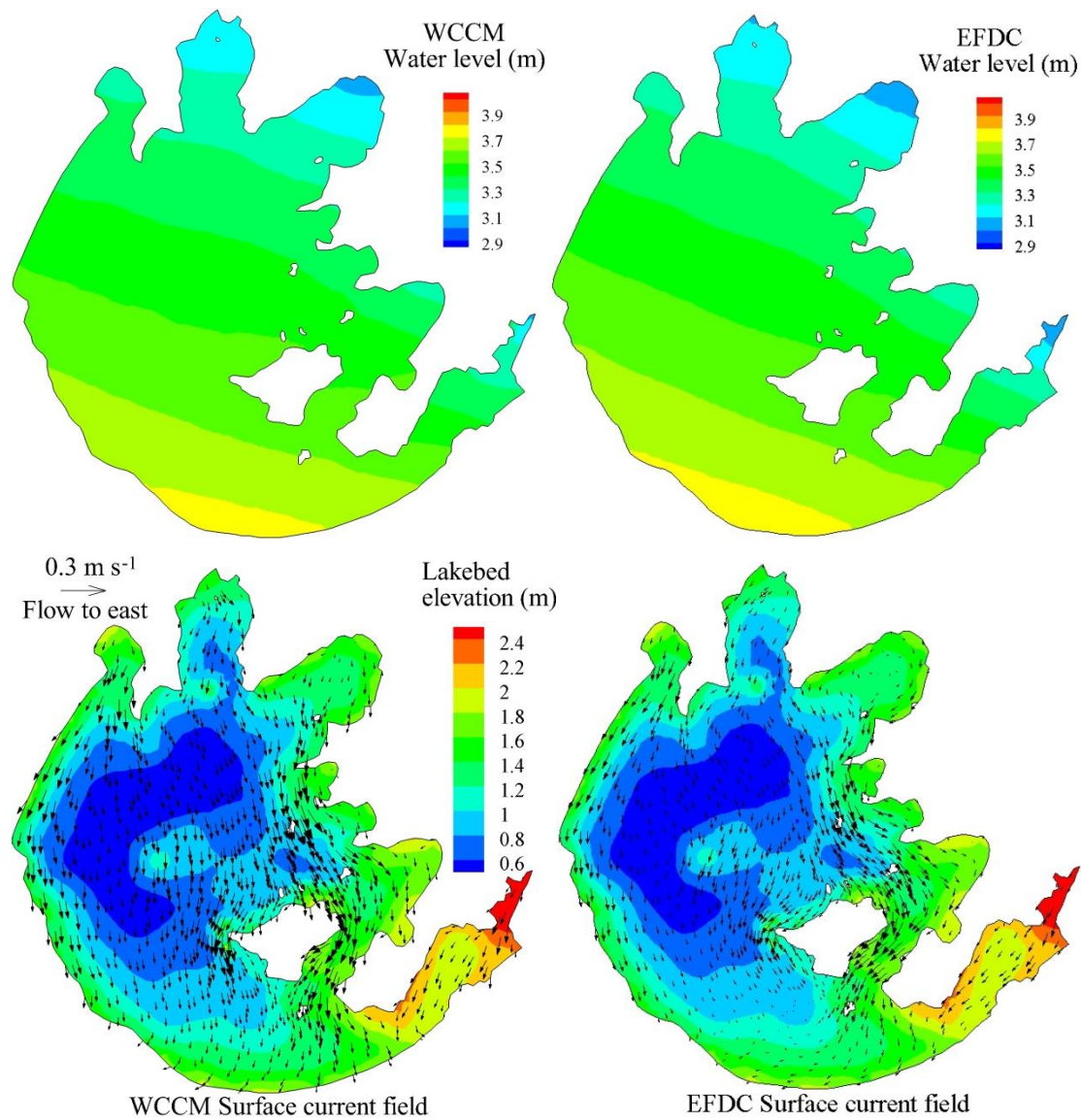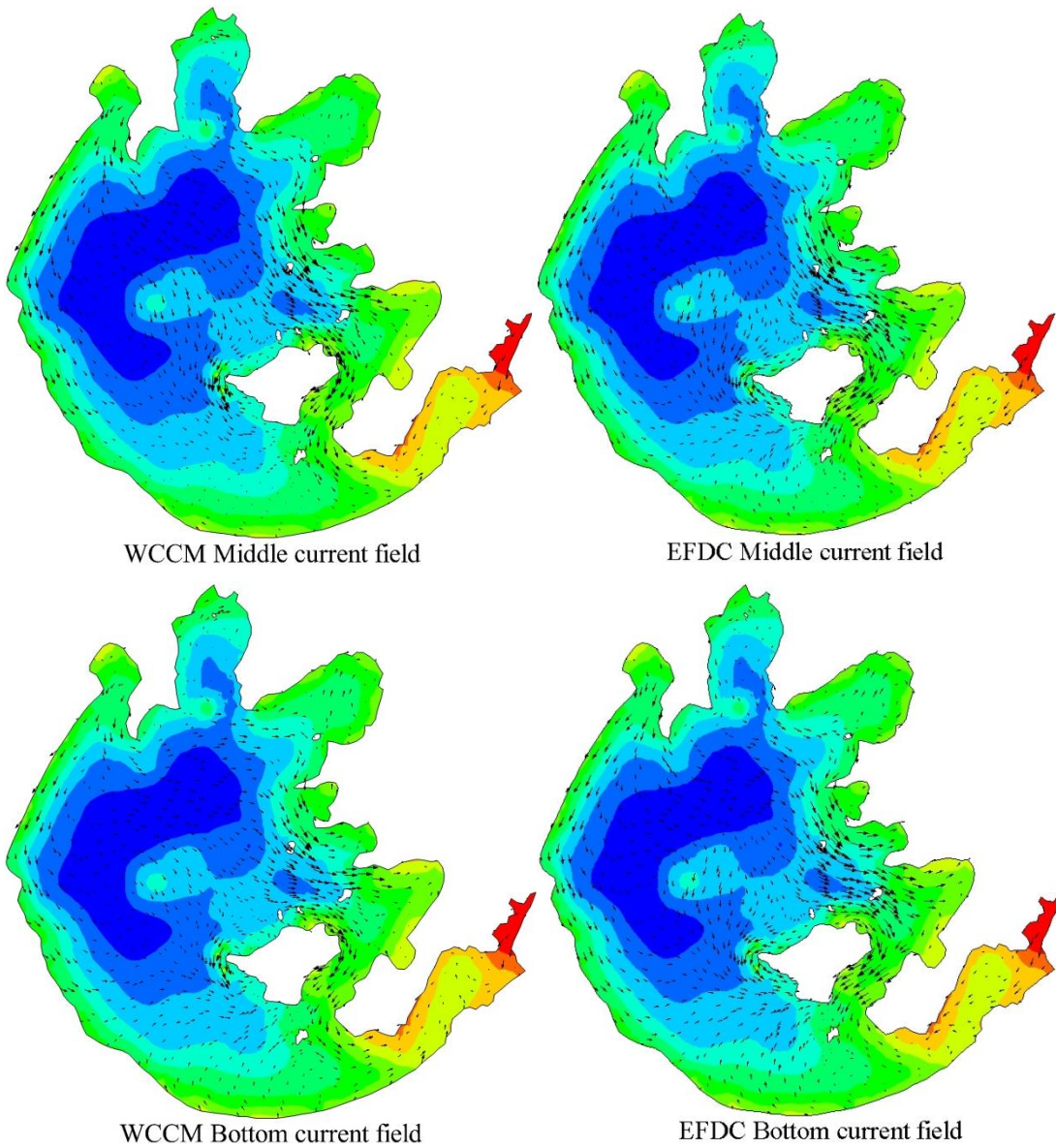
Figure 11: Comparison of the contour of the water level and surface, middle, and bottom current fields simulated by the WCCM with those simulated by the EFDC at 22:00 on December 26, 2018.

745

750

Appendix A

A1 Methods of coordinate transformation

$$\frac{\partial \Psi}{\partial x'} = \frac{\partial \Psi}{\partial x} - \frac{1}{H}\frac{\partial \Psi}{\partial \sigma}\left(\sigma\frac{\partial H}{\partial x} + \frac{\partial h}{\partial x}\right), \tag{A1-1}$$

$$\frac{\partial \Psi}{\partial y'} = \frac{\partial \Psi}{\partial y} - \frac{1}{H}\frac{\partial \Psi}{\partial \sigma}\left(\sigma\frac{\partial H}{\partial y} + \frac{\partial h}{\partial y}\right), \tag{A1-2}$$

755
$$\frac{\partial \Psi}{\partial z} = \frac{1}{H}\frac{\partial \Psi}{\partial \sigma}, \tag{A1-3}$$

$$\frac{\partial \Psi}{\partial t'} = \frac{\partial \Psi}{\partial t} - \frac{\sigma}{H}\frac{\partial \Psi}{\partial \sigma}\frac{\partial \zeta}{\partial t}, \tag{A1-4}$$

$$w' = Hw + \sigma\left(\frac{\partial \zeta}{\partial t} + u\frac{\partial \zeta}{\partial x} + v\frac{\partial \zeta}{\partial y}\right) + (1-\sigma)\left(u\frac{\partial h}{\partial x} + v\frac{\partial h}{\partial y}\right), \tag{A1-5}$$

where ψ is u, v, and w in the sigma coordinate system and w' is the vertical velocity in the Cartesian coordinate system, m s^{-1}.

A2 Secondary terms

760 $\varepsilon_U =$

$$-\frac{\partial}{\partial x}\left(A_H\frac{\partial u}{\partial \sigma}\right)\left(\sigma\frac{\partial H}{\partial x} + \frac{\partial h}{\partial x}\right) - \frac{\partial}{\partial \sigma}\left(A_H\frac{\partial u}{\partial x}\right)\left(\sigma\frac{\partial H}{\partial x} + \frac{\partial h}{\partial x}\right) + \frac{2A_H}{H}\frac{\partial u}{\partial \sigma}\frac{\partial H}{\partial x}\left(\sigma\frac{\partial H}{\partial x} + \frac{\partial h}{\partial x}\right) - A_H\frac{\partial u}{\partial \sigma}\left(\sigma\frac{\partial^2 H}{\partial x^2} + \frac{\partial^2 h}{\partial x^2}\right) + \frac{1}{H}\frac{\partial}{\partial \sigma}\left(A_H\frac{\partial u}{\partial \sigma}\right)\left(\sigma\frac{\partial H}{\partial x} + \right.$$
$$\left.\frac{\partial h}{\partial x}\right)^2 - \frac{\partial}{\partial y}\left(A_H\frac{\partial u}{\partial \sigma}\right)\left(\sigma\frac{\partial H}{\partial y} + \frac{\partial h}{\partial y}\right) - \frac{\partial}{\partial \sigma}\left(A_H\frac{\partial u}{\partial y}\right)\left(\sigma\frac{\partial H}{\partial y} + \frac{\partial h}{\partial y}\right) + \frac{2A_H}{H}\frac{\partial u}{\partial \sigma}\frac{\partial H}{\partial y}\left(\sigma\frac{\partial H}{\partial y} + \frac{\partial h}{\partial y}\right) - A_H\frac{\partial u}{\partial \sigma}\left(\sigma\frac{\partial^2 H}{\partial y^2} + \frac{\partial^2 h}{\partial y^2}\right) +$$
$$\frac{1}{H}\frac{\partial}{\partial \sigma}\left(A_H\frac{\partial u}{\partial \sigma}\right)\left(\sigma\frac{\partial H}{\partial y} + \frac{\partial h}{\partial y}\right)^2 + \frac{\rho g H}{\rho_0}\frac{\partial H}{\partial x}(1-\sigma) - \frac{g H^2}{\rho_0}\frac{\partial\left(\int_\sigma^1 \rho d\sigma\right)}{\partial x} - \frac{g H}{\rho_0}\frac{\partial H}{\partial x}\int_\sigma^1 \rho d\sigma, \tag{A2-1}$$

$\varepsilon_V =$

765
$$-\frac{\partial}{\partial x}\left(A_H\frac{\partial v}{\partial \sigma}\right)\left(\sigma\frac{\partial H}{\partial x} + \frac{\partial h}{\partial x}\right) - \frac{\partial}{\partial \sigma}\left(A_H\frac{\partial v}{\partial x}\right)\left(\sigma\frac{\partial H}{\partial x} + \frac{\partial h}{\partial x}\right) + \frac{2A_H}{H}\frac{\partial v}{\partial \sigma}\frac{\partial H}{\partial x}\left(\sigma\frac{\partial H}{\partial x} + \frac{\partial h}{\partial x}\right) - A_H\frac{\partial v}{\partial \sigma}\left(\sigma\frac{\partial^2 H}{\partial x^2} + \frac{\partial^2 h}{\partial x^2}\right) + \frac{1}{H}\frac{\partial}{\partial \sigma}\left(A_H\frac{\partial v}{\partial \sigma}\right)\left(\sigma\frac{\partial H}{\partial x} + \right.$$
$$\left.\frac{\partial h}{\partial x}\right)^2 - \frac{\partial}{\partial y}\left(A_H\frac{\partial v}{\partial \sigma}\right)\left(\sigma\frac{\partial H}{\partial y} + \frac{\partial h}{\partial y}\right) - \frac{\partial}{\partial \sigma}\left(A_H\frac{\partial v}{\partial y}\right)\left(\sigma\frac{\partial H}{\partial y} + \frac{\partial h}{\partial y}\right) + \frac{2A_H}{H}\frac{\partial v}{\partial \sigma}\frac{\partial H}{\partial y}\left(\sigma\frac{\partial H}{\partial y} + \frac{\partial h}{\partial y}\right) - A_H\frac{\partial v}{\partial \sigma}\left(\sigma\frac{\partial^2 H}{\partial y^2} + \frac{\partial^2 h}{\partial y^2}\right) +$$
$$\frac{1}{H}\frac{\partial}{\partial \sigma}\left(A_H\frac{\partial v}{\partial \sigma}\right)\left(\sigma\frac{\partial H}{\partial y} + \frac{\partial h}{\partial y}\right)^2 + \frac{\rho g H}{\rho_0}\frac{\partial H}{\partial y}(1-\sigma) - \frac{g H^2}{\rho_0}\frac{\partial\left(\int_\sigma^1 \rho d\sigma\right)}{\partial y} - \frac{g H}{\rho_0}\frac{\partial H}{\partial y}\int_\sigma^1 \rho d\sigma, \tag{A2-2}$$

$$B_U = -\frac{\partial \int_0^1 Huud\sigma}{\partial x} - \frac{\partial \int_0^1 Huvd\sigma}{\partial y} + fV + \int_0^1 F_x Hd\sigma + H\frac{\partial}{\partial x}\left(A_H\frac{\partial \int_0^1 ud\sigma}{\partial x}\right) + H\frac{\partial}{\partial y}\left(A_H\frac{\partial \int_0^1 ud\sigma}{\partial y}\right) + \frac{A_V}{H}\frac{\partial u}{\partial \sigma}\Big|_0^1 + \int_0^1 \varepsilon_U d\sigma, \tag{A2-3}$$

770

$$B_V = -\frac{\partial \int_0^1 Huv d\sigma}{\partial x} - \frac{\partial \int_0^1 Hvv d\sigma}{\partial y} + fU + \int_0^1 F_y H d\sigma + H\frac{\partial}{\partial x}\left(A_H \frac{\partial \int_0^1 v d\sigma}{\partial x}\right) + H\frac{\partial}{\partial y}\left(A_H \frac{\partial \int_0^1 v d\sigma}{\partial y}\right) + \frac{A_V}{H}\frac{\partial v}{\partial \sigma}\Big|_0^1 + \int_0^1 \varepsilon_V d\sigma, \quad \text{(A2-4)}$$

$$D_U = -\frac{\partial (Huu)}{\partial x} - \frac{\partial (Huv)}{\partial y} - \frac{\partial (Huw)}{\partial \sigma} + fHv + F_x H + H\frac{\partial}{\partial x}\left(A_H \frac{\partial u}{\partial x}\right) + H\frac{\partial}{\partial y}\left(A_H \frac{\partial u}{\partial y}\right) + \varepsilon_U - B_U, \quad \text{(A2-5)}$$

$$D_V = -\frac{\partial (Huv)}{\partial x} - \frac{\partial (Hvv)}{\partial y} - \frac{\partial (Hvw)}{\partial \sigma} - fHu + F_y H + H\frac{\partial}{\partial x}\left(A_H \frac{\partial v}{\partial x}\right) + H\frac{\partial}{\partial y}\left(A_H \frac{\partial v}{\partial y}\right) + \varepsilon_V - B_V, \quad \text{(A2-6)}$$

A3 Solution of equations

Using the splitting mode technique (Blumberg and Mellor, 1987) and alternation direction implicit algorithm (Butler, 1980), the external mode is derived by vertically integrating the momentum equations to solve the change in water surface which feedback the internal mode and solve the vertical current velocity. Equations (1)–(3) are vertically integrated, and $U = \int_0^1 Hu d\sigma$ and $V = \int_0^1 Hv d\sigma$ are used to represent the current speeds in the x- and y-directions. Equations (1)–(3) can then be transformed as follows:

$$\frac{\partial \zeta}{\partial t} + \frac{\partial U}{\partial x} + \frac{\partial V}{\partial y} = 0, \quad \text{(A3-1)}$$

$$\frac{\partial U}{\partial t} = -\frac{\rho g H}{\rho_0}\frac{\partial \zeta}{\partial x} + B_U, \quad \text{(A3-2)}$$

$$\frac{\partial V}{\partial t} = -\frac{\rho g H}{\rho_0}\frac{\partial \zeta}{\partial y} + B_V, \quad \text{(A3-3)}$$

where B_U and B_V are shown in Eqs. (A2-1) and (A2-2).

The expressions of the internal mode can be achieved using Eq. (2) minus Eq. (A3-2), and Eq. (3) minus Eq. (A3-3):

$$\frac{\partial (Hu')}{\partial t} = \frac{1}{H}\frac{\partial}{\partial \sigma}\left(A_V \frac{\partial \left(u' + \frac{U}{H}\right)}{\partial \sigma}\right) + D_U, \quad \text{(A3-4)}$$

$$\frac{\partial (Hv')}{\partial t} = \frac{1}{H}\frac{\partial}{\partial \sigma}\left(A_V \frac{\partial \left(v' + \frac{V}{H}\right)}{\partial \sigma}\right) + D_V, \quad \text{(A3-5)}$$

Where $u' = u - \frac{U}{H}$, $v' = v - \frac{V}{H}$, and D_U and D_V are shown in Eqs. (A2-5) and (A2-6).

These equations are discretized using the finite difference method. For the external mode equations, the alternation direction implicit difference scheme and staggered grid (Figs. 2, 3) are used to discretize Eqs. (A3-1) and (A3-2) and then obtain the equation to calculate U in the next time increment:

$$\zeta_{i,j}^{n+\frac{1}{2}} + (1-\alpha)\Delta t \frac{\partial U}{\partial x}\Big|_{i,j}^{n+1} = \zeta_{i,j}^n - \alpha \Delta t \frac{\partial U}{\partial x}\Big|_{i,j}^n - \Delta t \frac{\partial V}{\partial y}\Big|_{i,j}^n, \quad \text{(A3-6)}$$

$$(1-\alpha)gH\Delta t \frac{\partial \zeta}{\partial x}\Big|_{i+\frac{1}{2},j}^{n+\frac{1}{2}} + U_{i+\frac{1}{2},j}^{n+1} = -\alpha gH\Delta t \frac{\partial \zeta}{\partial x}\Big|_{i+\frac{1}{2},j}^n + U_{i+\frac{1}{2},j}^n + \Delta t B_U\Big|_{i+\frac{1}{2},j}^n, \quad \text{(A3-7)}$$

37

where α is the format weight coefficient. When $\alpha = 1$, Eqs. (A3-6) and (A3-7) are explicit; otherwise, they are implicit. The definition of each variable on the staggered grid is shown in Figs. 2 and 3.

According to the U value in next time increment, ζ and V can be calculated by:

$$\zeta_{i,j}^{n+1} + (1-\alpha)\Delta t \frac{\partial V}{\partial y}\Big|_{i,j}^{n+1} = \zeta_{i,j}^{n} - \alpha\Delta t \frac{\partial V}{\partial y}\Big|_{i,j}^{n} - \Delta t \frac{\partial U}{\partial x}\Big|_{i,j}^{n+1}, \tag{A3-8}$$

800

$$(1-\alpha)gH\Delta t \frac{\partial \zeta}{\partial y}\Big|_{i,j+\frac{1}{2}}^{n+1} + V_{i,j+\frac{1}{2}}^{n+1} = -\alpha gH\Delta t \frac{\partial \zeta}{\partial y}\Big|_{i,j+\frac{1}{2}}^{n} + V_{i,j+\frac{1}{2}}^{n} + \Delta t B_V\Big|_{i,j+\frac{1}{2}}^{n}, \tag{A3-9}$$

Similarly, the alternation direction implicit difference scheme is used to discretize Eqs. (A3-4) and (A3-5) of the internal mode to obtain:

$$0.5\left(H_{i+1,j}^{n+1} + H_{i,j}^{n+1}\right)u'\Big|_{i+\frac{1}{2},j,k}^{n+1} - (1-\alpha)\frac{\Delta t}{H}\frac{\partial}{\partial\sigma}\left(A_V \frac{\partial\left(u'+\frac{U}{H}\right)}{\partial\sigma}\right)\Big|_{i+\frac{1}{2},j,k}^{n+1} =$$

$$0.5\left(H_{i+1,j}^{n} + H_{i,j}^{n}\right)u'\Big|_{i+\frac{1}{2},j,k}^{n} + \alpha\frac{\Delta t}{H}\frac{\partial}{\partial\sigma}\left(A_V \frac{\partial\left(u'+\frac{U}{H}\right)}{\partial\sigma}\right)\Big|_{i+\frac{1}{2},j,k}^{n} + \Delta t D_U\Big|_{i+\frac{1}{2},j,k}^{n}, \tag{A3-10}$$

805

$$0.5\left(H_{i,j+1}^{n+1} + H_{i,j}^{n+1}\right)v'\Big|_{i,j+\frac{1}{2},k}^{n+1} - (1-\alpha)\frac{\Delta t}{H}\frac{\partial}{\partial\sigma}\left(A_V \frac{\partial\left(v'+\frac{V}{H}\right)}{\partial\sigma}\right)\Big|_{i,j+\frac{1}{2},k}^{n+1} =$$

$$0.5\left(H_{i,j+1}^{n} + H_{i,j}^{n}\right)v'\Big|_{i,j+\frac{1}{2},k}^{n} + \alpha\frac{\Delta t}{H}\frac{\partial}{\partial\sigma}\left(A_V \frac{\partial\left(v'+\frac{V}{H}\right)}{\partial\sigma}\right)\Big|_{i,j+\frac{1}{2},k}^{n} + \Delta t D_V\Big|_{i,j+\frac{1}{2},k}^{n}, \tag{A3-11}$$

The chasing algorithm is used to solve the tridiagonal matrix formed by Eqs. (A3-10 and A3-11). The current numerical model was built based on these governing equations and written in Intel Visual Fortran (Intel Inc. USA).

810

815

820

Appendix B
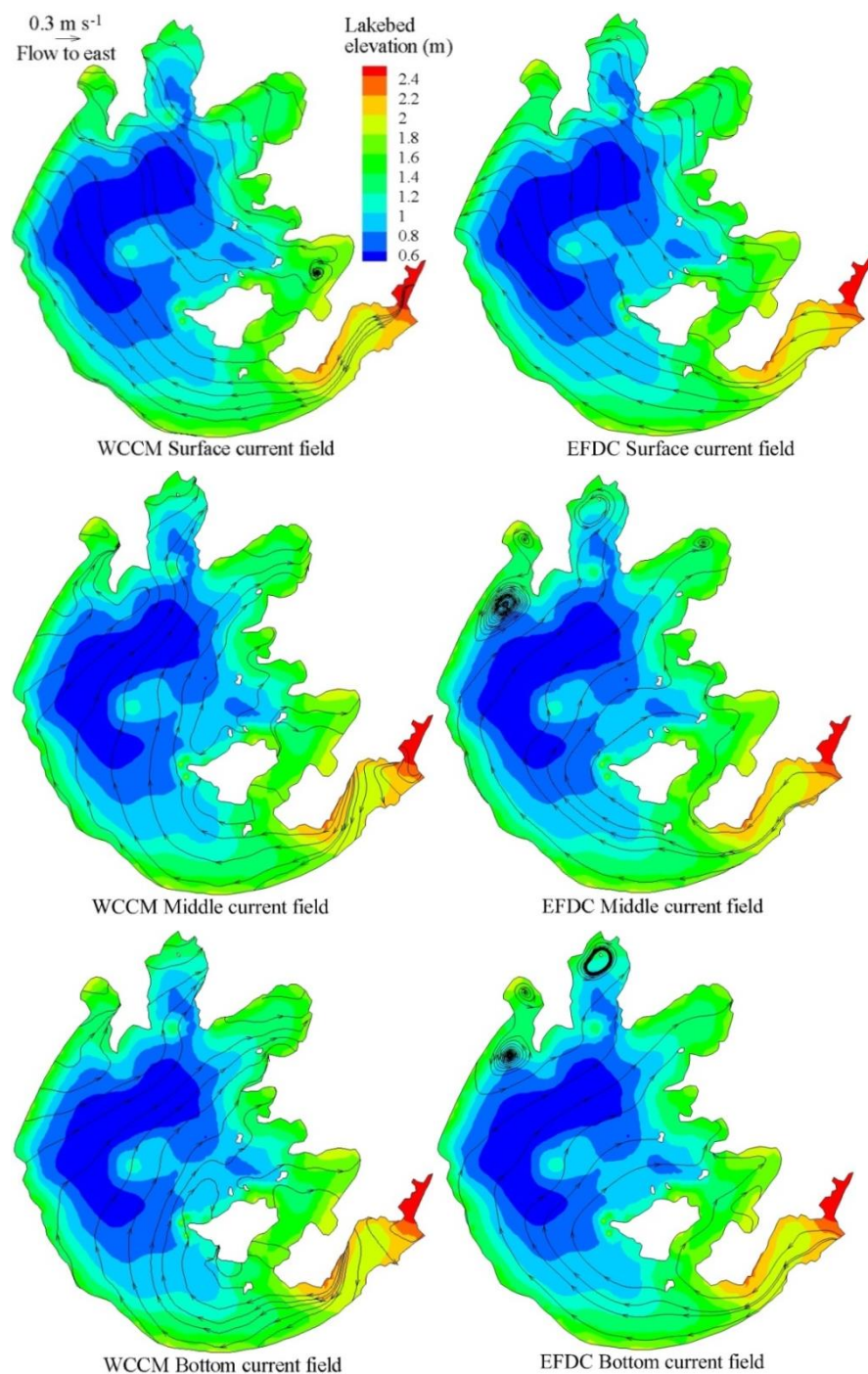
Fig. B.1 Comparison of the flow fields and stream traces in the surface, middle, and bottom layers of Lake Taihu simulated by the WCCM and EFDC at 12:00 on August 10, 2015

825
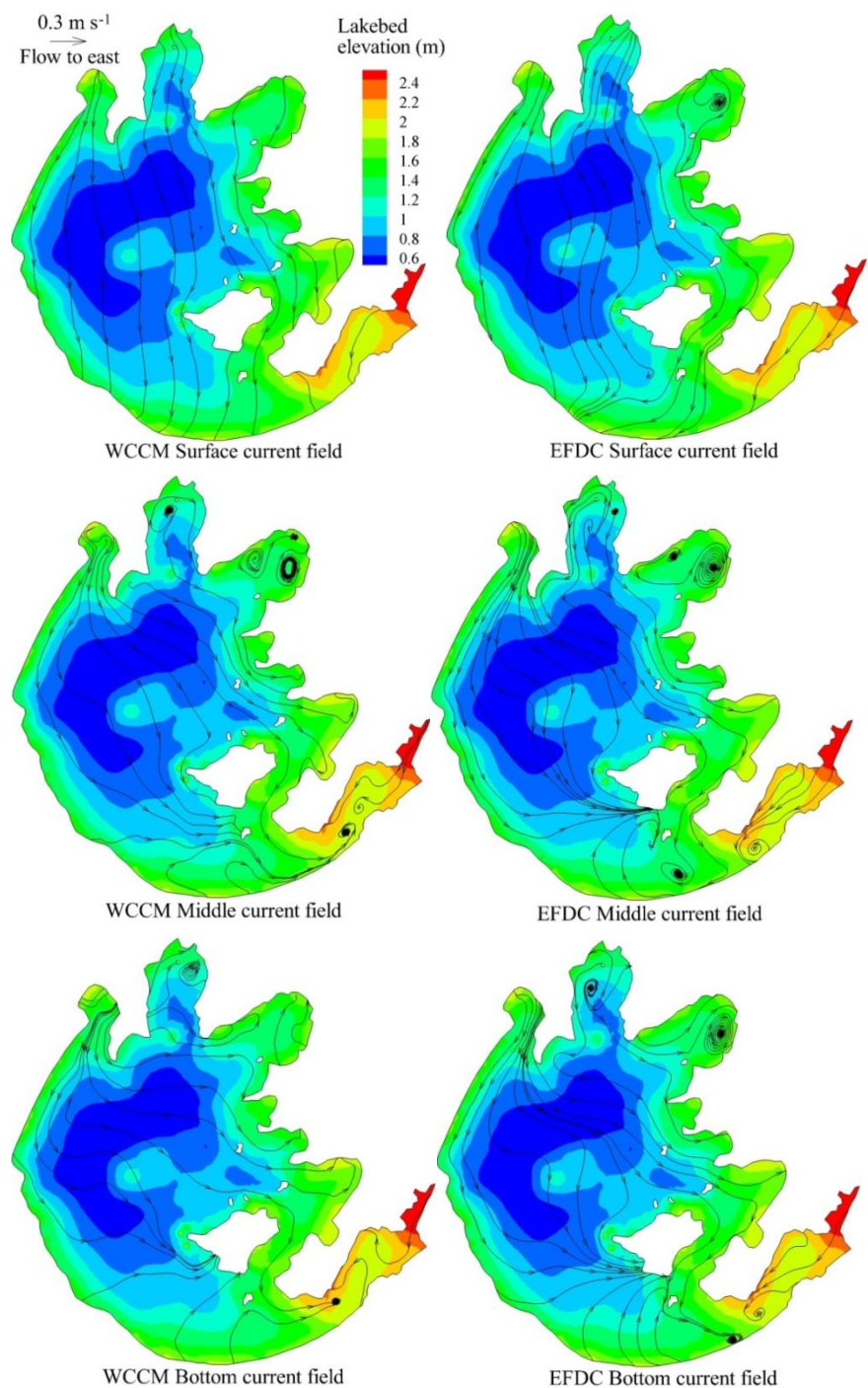
830

Fig. B.2 Comparison of the flow fields and stream traces in the surface, middle, and bottom layers of Lake Taihu simulated by the WCCM and EFDC at 22:00 on December 26, 2018.
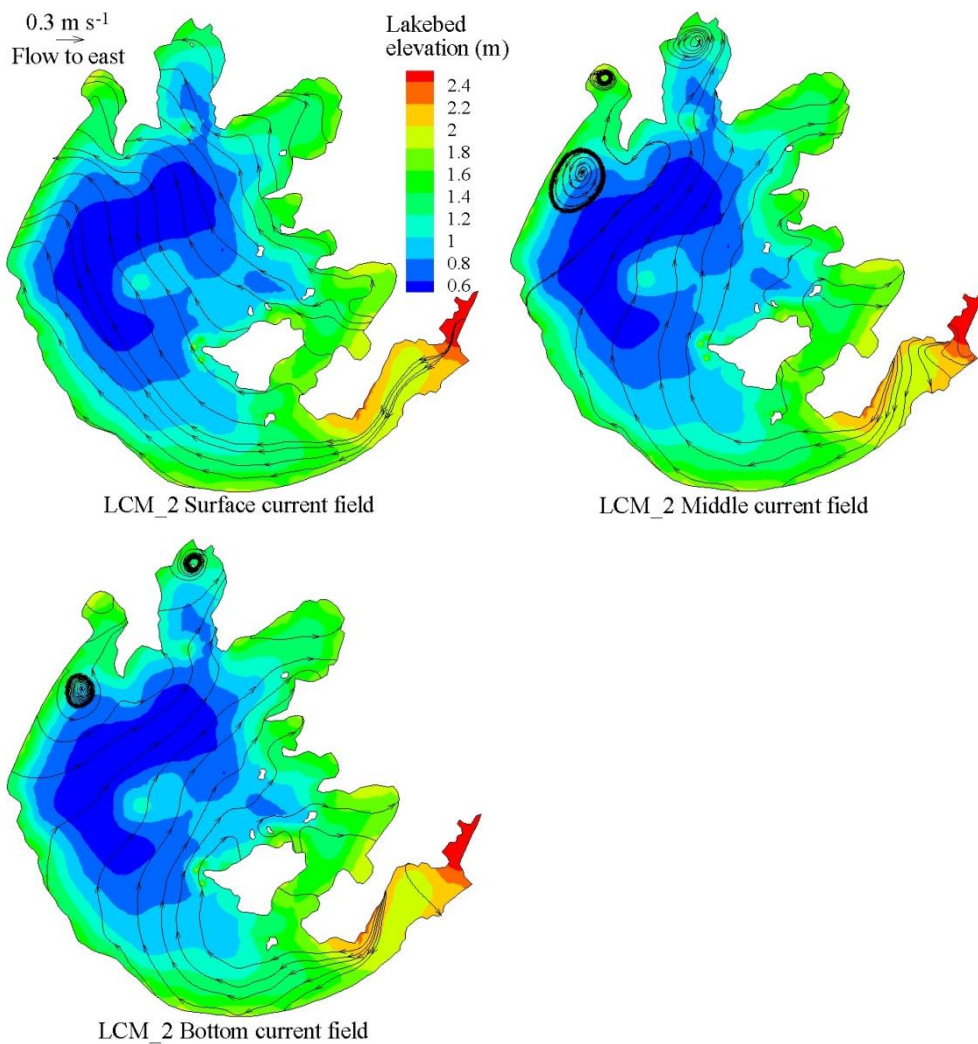
Fig.B.3 Comparison of the LCM_2-simulated streamtraces of the surface, middle, and bottom current fields in Lake Taihu at 12:00 on August 10, 2015